Computers and Mathematics with Applications 146 (2023) 339–359

Contents lists available at ScienceDirect

Computers and Mathematics with Applications

journal homepage: www.elsevier.com/locate/camwa

High order structure-preserving arbitrary Lagrangian-Eulerian discontinuous Galerkin methods for the Euler equations under gravitational fields

Weijie Zhang [a,1], Yulong Xing [b,2], Yinhua Xia [a,3], Yan Xu [a,*,4]

[a] School of Mathematical Sciences, University of Science and Technology of China, Hefei, Anhui 230026, PR China
[b] Department of Mathematics, The Ohio State University, Columbus, OH 43210, USA

ARTICLE INFO

Keywords:
Euler equations
Arbitrary Lagrangian-Eulerian
Discontinuous Galerkin methods
Positivity-preserving
Well-balanced
Gravitational field

ABSTRACT

In this work, we present high-order arbitrary Lagrangian-Eulerian discontinuous Galerkin (ALE-DG) methods for the Euler equations under gravitational fields on the moving mesh. The goal of this paper is to demonstrate that, through careful design of the scheme, the ALE-DG methods can also achieve the structure-preserving properties of DG methods, such as high order accuracy, well-balanced property, positivity-preserving property, for the Euler equations with arbitrary moving meshes. We propose two well-balanced and positivity-preserving ALE-DG schemes which can preserve the explicitly given equilibrium state on arbitrary moving grids, and also carry out rigorous positivity-preserving analyses for both schemes. Our schemes are established both in one dimension and in two dimensions on unstructured triangular meshes. The most challenging component in designing such ALE-DG schemes on the moving mesh is to maintain the equilibrium state and the mass conservation at the same time, since temporal discretization of the ALE method may destroy the well-balanced property, and inappropriate adjustment of the numerical flux could lead to the loss of the mass conservation property on the moving meshes. A novel approximation of the desired equilibrium state based on ALE-DG methods on the moving mesh has been introduced to overcome such difficulty. Numerical experiments in different circumstances are provided to illustrate the well-balanced property, positivity-preserving property and high order accuracy. We also compare the schemes on the moving mesh and on the static mesh to demonstrate the advantage of ALE-DG methods for discontinuous solutions.

1. Introduction

In this paper, we consider the compressible Euler equations with gravitation in d-dimensions, which take the form

$$\begin{aligned} &\rho_t + \nabla\cdot\boldsymbol{m} = 0,\\ &\boldsymbol{m}_t + \nabla\cdot\left(\frac{\boldsymbol{m}\otimes\boldsymbol{m}}{\rho} + pI\right) = -\rho\nabla\phi,\\ &E_t + \nabla\cdot\left((E+p)\frac{\boldsymbol{m}}{\rho}\right) = -\boldsymbol{m}\cdot\nabla\phi. \end{aligned} \tag{1.1}$$

Here, $\rho > 0$ denotes the density, $\boldsymbol{m} = \rho\boldsymbol{u} \in \mathbb{R}^d$ is the momentum vector, $\boldsymbol{u} \in \mathbb{R}^d$ is the velocity vector, $p > 0$ is the pressure, $E = \rho e + \frac{1}{2}\rho\|\boldsymbol{u}\|^2$ is the non-gravitational energy and $\phi(\boldsymbol{x})$ denotes the time independent gravitational potential. The system is closed by an equation of state (EoS) of the form $p = p(\rho, e)$, which links the pressure p to the density ρ and the internal energy e. The ideal EoS is given by

$$p = (\gamma - 1)\rho e, \tag{1.2}$$

where γ is the ratio of specific heat.

* Corresponding author.
E-mail addresses: zhwj@mail.ustc.edu.cn (W. Zhang), xing.205@osu.edu (Y. Xing), yhxia@ustc.edu.cn (Y. Xia), yxu@ustc.edu.cn (Y. Xu).

[1] This work was carried out when W. Zhang was visiting Department of Mathematics, The Ohio State University.
[2] The work of Y. Xing is partially supported by the NSF grant DMS-1753581.
[3] Research supported by NSFC grant No. 12271498, 11871449 and National Key R&D Program of China No. 2022YFA1005202/2022YFA1005200.
[4] Research supported by NSFC grant No. 12071455, 11722112.

https://doi.org/10.1016/j.camwa.2023.07.029
Received 27 September 2022; Received in revised form 28 June 2023; Accepted 28 July 2023

The Euler system in (1.1) has wide applications in modeling physical phenomena such as astrophysical and atmospheric phenomena. They also admit a general hydrostatic equilibrium state where the flux gradient exactly balances the gravitational source term and the velocity vector equals zero:

$$\boldsymbol{u} = 0, \quad \nabla p = -\rho \nabla \phi. \tag{1.3}$$

Two well-known hydrostatic equilibrium states are the isothermal and the polytropic equilibria. In many practical simulations, the flows under consideration can be viewed as small perturbations of these equilibrium states. The well-balanced schemes are introduced to properly capture this type of flow, which often appears in astrophysical and atmospheric applications. One major advantage of the well-balanced schemes is that they can effectively and accurately resolve these small perturbations of equilibrium states on relatively coarse meshes. The well-balanced methods have been widely studied in the few past decades, especially for the shallow water equations with non-flat bottom topography. Earlier works in this field include [5,26,3,1], and high-order well-balanced schemes have been designed to preserve still water equilibria [40,44,16] and moving water equilibria [39] of the shallow water equations. We refer to the review papers [43,25] and the references therein. For the compressible Euler equations under gravitation fields, the well-balanced methods are more complicated and have attracted much attention recently. They were first introduced by LeVeque and Bale in [27]. Later, well-balanced schemes were studied for isothermal equilibrium states in [42] and polytropic equilibrium states in [21]. After that, there are many well-balanced methods developed within several different frameworks, which can preserve the zero velocity equilibrium states, e.g. [29,8,28,9,23,38,22,7,33,37].

Another important difficulty in numerical simulations for the Euler equations is preserving the positivity of density and pressure. Physically, the density ρ and the pressure p should both stay positive. The appearance of negative density or pressure in the numerical methods may lead to difficulty in the simulation. There have been extensive studies of first or second order positivity-preserving schemes up to second order in the earlier work [13,35]. In recent years, many high-order bound-preserving schemes have been studied for hyperbolic conservation laws [18,50,46]. Two popular approaches have been reviewed in the recent paper [47]. The first one is through the design of a simple scaling limiter for finite volume and discontinuous Galerkin schemes. Using this approach, high-order positivity-preserving DG schemes were designed for Euler equations without source term [50,52] and with source terms [51]. The second approach is to introduce a bound-preserving flux limiter as discussed in [46,45].

The arbitrary Lagrangian-Eulerian (ALE) methods with moving meshes have been widely used in solid mechanics and for problems involving moving boundaries. ALE finite element methods for the incompressible Navier-Stokes equations have been proposed in [11,20]. Recently, arbitrary Lagrangian-Euler discontinuous Galerkin (ALE-DG) methods have been designed for solving compressible flows in [30,34,32]. The theoretical analysis of ALE-DG schemes coupled with Runge-Kutta time stepping has been introduced in [24] in one dimension and extended to two dimensions in [14]. By adopting the time-dependent linear affine mapping, the ALE-DG method for conservation laws maintains almost all mathematical properties of DG methods on static grids, such as conservation, geometric conservation law (GCL), maximum principle preserving property, and optimal error estimates.

There are two popular strategies to update the computational mesh in the ALE methods. The first one is similar to the classical Lagrangian methods, where the grid velocity is selected as the local fluid velocity [2,15]. Such an approach can track the moving boundaries or minimize the numerical dissipation. The second one involves a monitor function and will concentrate the grids in zones where the solution demonstrates large gradients [19,31]. We refer to [12] and the references therein for more details about ALE methods.

Numerical methods, which can satisfy both the well-balanced property and the positivity-preserving property for the Euler equations with gravitation, have been studied in a few recent works within the framework of finite volume [36] and finite element DG methods [38,49]. The main objective of this paper is to extend these schemes to moving meshes, and study well-balanced positivity-preserving ALE-DG schemes to enjoy the benefits of moving mesh methods. This paper concentrates on the design of numerical methods and aims to show that ALE-DG methods can achieve nice properties on arbitrarily moving meshes: high order accuracy, well-balanced and positivity-preserving properties. The strategy of mesh movements was not considered in this paper. We notice that the well-balanced positivity-preserving DG methods cannot be generalized to ALE-DG methods in a straightforward way. The main challenge is that the standard Total Variational Diminishing Runge-Kutta (TVD-RK) time discretization may destroy the well-balanced property on moving mesh. The well-balanced positivity-preserving ALE-DG methods were studied in [48] for the shallow water equations. To overcome this challenge, one important technique in this paper is the novel approximation of the bottom topography or the equilibrium state based on ALE-DG methods. In [15], an ALE finite volume scheme has been developed in the cylindrical coordinates, which is well-balanced if the mesh satisfies some special conditions. To obtain the well-balanced property on arbitrary moving mesh, one needs to define the approximation equilibrium state on the moving mesh carefully. Another challenge is maintaining mass conservation, which becomes a nontrivial thing as the grid velocity is now incorporated into the fluxes. In addition, improper handling of this term may also destroy the positivity-preserving property. To overcome these difficulties, we first assume that the desired equilibrium state is explicitly given and then introduce a novel approximation for that known equilibrium based on the ALE-DG scheme, which is similar to [48]. We aim to numerically preserve a special projection of this equilibrium solution on moving meshes, which may slightly change on different meshes. The objective of the well-balanced property is to maintain the error between the numerical solution and this projection to machine error, and demonstrate that our proposed methods can help capture small perturbations. Two schemes have been proposed in this paper, based on different well-balanced strategies, and they have very different proofs of the positivity-preserving property. The first one is via the hydrostatic reconstruction, which is first introduced in [1] for solving the shallow water equations and then extended to Euler equations in [29]. The second approach is by reformulating the source term and utilizing the properties of HLLC flux as studied in [38]. We will start by describing these algorithms in detail, and then rigorously prove these schemes' well-balanced property and positivity-preserving property. The advantage of the ALE-DG method on moving meshes will also be demonstrated in the numerical examples.

The rest of the paper is organized as follows. In Section 2, we present the standard ALE-DG settings for solving Euler equations. In Section 3, we first introduce the desired equilibrium states and the admissible states for Euler equations with gravitation. Two well-balanced ALE-DG schemes for the Euler equations with gravitation, which preserve both the isothermal and the polytropic equilibrium states, will be presented. In Section 4, the positivity-preserving property of the proposed methods will be investigated. In Section 5, we provide extensive one- and two-dimensional numerical examples to validate the well-balanced property, high order accuracy, the advantages of ALE-DG methods, and positivity-preserving property on moving meshes. We give some concluding remarks in Section 6. The detailed proof of the weak positivity property will be elaborated in Appendix A and Appendix B.

2. The ALE-DG methods

In this section, we briefly discuss some notations and setups involved in the study of ALE-DG methods, and refer to [14] for more details and discussions on them.

2.1. Time-dependent cells and grid velocity field

For ALE-DG methods, the computational mesh can be changed over each time step. We assume that $\Omega \in \mathbb{R}^d$ is the computational domain and $\mathcal{T}^n$ is a mesh of the domain Ω at the time step t^n, such that

$$\Omega = \bigcup \{ K^n \mid K^n \in \mathcal{T}^n \}, \tag{2.1}$$

where all the elements K^n are the simplex cells. Suppose that $\boldsymbol{x}_0^n$ and $\boldsymbol{x}_0^{n+1}$ are the coordinates of the same mesh grid at time t^n and t^{n+1} respectively. We can define the grid velocity on this mesh grid as

$$\boldsymbol{\omega}_0^n := \frac{\boldsymbol{x}_0^{n+1} - \boldsymbol{x}_0^n}{t^{n+1} - t^n}, \tag{2.2}$$

and connect them with a straight line

$$\boldsymbol{x}_0(t) := \boldsymbol{x}_0^n + \boldsymbol{\omega}_0^n (t - t^n). \tag{2.3}$$

For any given fixed time $t \in [t^n, t^{n+1}]$, we can evaluate the new coordinate of the mesh grids using this. By maintaining their connectivity, we can obtain the moving mesh $\mathcal{T}(t)$ and time-dependent computational cells $K(t)$ for $t \in [t^n, t^{n+1}]$

$$\Omega = \bigcup \{ K(t) \mid K(t) \in \mathcal{T}(t) \}, \quad K(t) := \mathrm{conv}\left\{ \boldsymbol{x}_{K,1}(t), \cdots, \boldsymbol{x}_{K,d+1}(t) \right\}, \tag{2.4}$$

where $\boldsymbol{x}_{K,1}(t), \cdots, \boldsymbol{x}_{K,d+1}(t)$ are the vertices of $K(t)$ and conv$(\cdot)$ denotes the convex hull of a set. We denote the edges of $K(t)$ by $F^{\nu}_{K(t)}$, $\nu = 1, \cdots, d+1$, such that

$$\partial K(t) := \bigcup_{\nu=1}^{d+1} F^{\nu}_{K(t)}. \tag{2.5}$$

The volume of $K(t)$ is denoted by $\Delta_{K(t)}$.

Note that we plan to compute the numerical solution at time t^{n+1} on a mesh $\mathcal{T}^{n+1}$, by using the numerical solution at time t^n on a different mesh $\mathcal{T}^n$. Therefore, the grid velocity was used to derive the numerical scheme. Next, we are ready to define the grid velocity field $\boldsymbol{\omega}_K(\boldsymbol{x}, t)$ for time $t \in [t^n, t^{n+1}]$. We assume that the grid velocity $\boldsymbol{\omega}_K(\boldsymbol{x}, t)$ is a vector with d components, and its components are denoted by $\omega_K^{[i]}(\boldsymbol{x}, t)$, $i = 1, \cdots, d$. The main principle for the meshes at different time steps is that the topography of the mesh should be unchanged and only the position of the grids can be changed. In such a case, we can assume the corresponding grids are connected by straight lines and the grid velocity for each point in time interval $[t^n, t^{n+1}]$ is constant. We also assume that the grid velocity in each spatial cell is a linear polynomial, so that the grid velocity of vertices can determine the grid velocity of any point inside the spatial cell. Under this assumption, the following $d+2$ points are coplanar: $(\boldsymbol{x}_{K,1}^n, \omega_{K,1}^{n,[i]}), \cdots, (\boldsymbol{x}_{K,d+1}^n, \omega_{K,d+1}^{n,[i]}), (\boldsymbol{x}_K^n(\boldsymbol{x}), \omega_K^{n,[i]}(\boldsymbol{x}))$. Therefore, on cell K, the linear polynomials $\omega_K^{[i]}(\boldsymbol{x}, t)$, $i = 1, \cdots, d$, can be solved by the following equation

$$\begin{vmatrix} \boldsymbol{x} - \boldsymbol{x}_{K,1}(t) & \boldsymbol{x}_{K,2}(t) - \boldsymbol{x}_{K,1}(t) & \cdots & \boldsymbol{x}_{K,d+1}(t) - \boldsymbol{x}_{K,1}(t) \\ \omega_K^{[i]}(\boldsymbol{x}, t) - \omega_{K,1}^{n,[i]} & \omega_{K,2}^{n,[i]} - \omega_{K,1}^{n,[i]} & \cdots & \omega_{K,d+1}^{n,[i]} - \omega_{K,1}^{n,[i]} \end{vmatrix} = 0. \tag{2.6}$$

Here $|\cdot|$ denotes the determinant of the $(d+1) \times (d+1)$ matrix, and $\boldsymbol{x}_{K,j}(t)$, $j = 1, \cdots, d$ are the vertexes of the cell K. $\boldsymbol{\omega}_{K,j}^n$, $j = 1, \cdots, d$ are the grid velocities on these vertexes as defined in (2.2), and $\omega_{K,j}^{n,[i]}$ denotes the i-th component of $\boldsymbol{\omega}_{K,j}^n$.

2.2. The time-dependent finite element space

We first introduce the time-independent reference cell

$$K_{\mathrm{ref}} := \left\{ \boldsymbol{\xi} = (\xi_1, \cdots, \xi_d)^T \in \mathbb{R}^d \;\middle|\; \xi_i \geq 0, \forall\, i \text{ and } \sum_{i=1}^{d} \xi_i \leq 1 \right\}, \tag{2.7}$$

which, in two dimensions, is a triangular element. The affine linear time-dependent mapping between this time-independent reference cell and the time-dependent cell in physical space (2.4) is denoted by

$$\chi_{K(t)} : K_{\mathrm{ref}} \to K(t), \quad \boldsymbol{\xi} \mapsto \chi_{K(t)}(\boldsymbol{\xi}, t) := \boldsymbol{A}_{K(t)} \boldsymbol{\xi} + \boldsymbol{x}_{K,1}(t), \tag{2.8}$$

where the matrix $\boldsymbol{A}_{K(t)}$ is given by

$$\boldsymbol{A}_{K(t)} := \Big(\boldsymbol{x}_{K,2}(t) - \boldsymbol{x}_{K,1}(t), \ \cdots, \boldsymbol{x}_{K,d+1}(t) - \boldsymbol{x}_{K,1}(t) \Big). \tag{2.9}$$

With the affine linear time-dependent mapping, we can define the time-dependent finite element space, to which the test function belongs, as

$$\mathcal{V}_d^k(t) := \left\{ \boldsymbol{\varphi} \in \left(L^2(\Omega(t)) \right)^{d+2} \;\middle|\; \boldsymbol{\varphi} \circ \chi_{K(t)} \in \left(\mathbb{P}^k(K_{\mathrm{ref}}) \right)^{d+2}, \ \forall K(t) \in \mathcal{T}(t) \right\}, \tag{2.10}$$

where $\mathbb{P}^k$ is the space of polynomials of degree no greater than k and $d+2$ refers to the number of equations in the Euler system. We establish the connection between test functions at different times: if two test functions, $\boldsymbol{\varphi}(\boldsymbol{x}, t)$ at time t and $\tilde{\boldsymbol{\varphi}}(\boldsymbol{x}, \tilde{t})$ at time $\tilde{t}$, satisfy that

$$\boldsymbol{\varphi}(\chi_{K(t)}(\boldsymbol{\xi}), t) = \tilde{\boldsymbol{\varphi}}(\chi_{K(\tilde{t})}(\boldsymbol{\xi}), \tilde{t}), \text{ for all } \boldsymbol{\xi} \in K_{\mathrm{ref}} \text{ and any cell } K, \tag{2.11}$$

we call them the corresponding test functions.

We also define the cell boundary values as

$$\boldsymbol{\varphi}^{int_{K(t)}}(\boldsymbol{x}) := \lim_{\epsilon \to 0^+} \boldsymbol{\varphi}\left(\boldsymbol{x} - \epsilon \boldsymbol{n}^{\nu}_{K(t)} \right), \quad \boldsymbol{\varphi}^{int_{K(t)}}(\boldsymbol{x}) := \lim_{\epsilon \to 0^+} \boldsymbol{\varphi}\left(\boldsymbol{x} + \epsilon \boldsymbol{n}^{\nu}_{K(t)} \right), \tag{2.12}$$

where $\boldsymbol{n}^{\nu}_{K(t)}$, $\nu = 1, \cdots, d+1$ denote the outer normal vector of $K(t)$ with respect to the simplex face $F^{\nu}_{K(t)}$.

2.3. The semi-discrete ALE-DG scheme

The conventional ALE-DG methods will be introduced in this subsection. We first write the compact form of equations (1.1) as

$$\boldsymbol{U}_t + \nabla \cdot \boldsymbol{F}(\boldsymbol{U}) = \boldsymbol{S}(\boldsymbol{U}, \nabla \phi), \tag{2.13}$$

where $\boldsymbol{U} = (\rho, \boldsymbol{m}, E)^T$, $\boldsymbol{F}(\boldsymbol{U})$ denotes the flux term and $\boldsymbol{S}(\boldsymbol{U}, \nabla \phi)$ is the source term. The standard ALE-DG scheme for the Euler equations with gravitation (2.13) is described as follows: find the numerical solution $\boldsymbol{U} \in \mathcal{V}_d^k(t)$, such that the equations

$$\frac{\mathrm{d}}{\mathrm{d}t} \int_{K(t)} \boldsymbol{U} \cdot \boldsymbol{\varphi} \mathrm{d}\boldsymbol{x} = \boldsymbol{\mathcal{L}}_K(\boldsymbol{\omega}, \boldsymbol{U}, \boldsymbol{\varphi}, t), \tag{2.14}$$

holds for any $\boldsymbol{\varphi} \in \mathcal{V}_d^k(t)$, with the spatial operator defined as

$$\begin{aligned} &\boldsymbol{\mathcal{L}}_K(\boldsymbol{\omega}, \boldsymbol{U}, \boldsymbol{\varphi}, t) \\ &= \int_{K(t)} \boldsymbol{G}(\boldsymbol{\omega}, \boldsymbol{U}) : \nabla \boldsymbol{\varphi} \mathrm{d}\boldsymbol{x} - \int_{\partial K(t)} \hat{\boldsymbol{G}}\left(\boldsymbol{\omega}, \boldsymbol{U}^{int}, \boldsymbol{U}^{ext}, \boldsymbol{n} \right) \cdot \boldsymbol{\varphi} \mathrm{d}s \\ &\quad + \int_{K(t)} \boldsymbol{S}(\boldsymbol{U}, \nabla \phi) \cdot \boldsymbol{\varphi} \mathrm{d}\boldsymbol{x}, \end{aligned} \tag{2.15}$$

where

- the flux $\boldsymbol{G}$ of the ALE-DG methods is defined as follows

$$\boldsymbol{G}(\boldsymbol{\omega}, \boldsymbol{U}) := \boldsymbol{F}(\boldsymbol{U}) - \boldsymbol{\omega} \otimes \boldsymbol{U} = \begin{pmatrix} \rho(\boldsymbol{u} - \boldsymbol{\omega}) \\ \boldsymbol{m} \otimes (\boldsymbol{u} - \boldsymbol{\omega}) + p I \\ E(\boldsymbol{u} - \boldsymbol{\omega}) + p \boldsymbol{u} \end{pmatrix}, \tag{2.16}$$

  and the operator $\otimes$ is the tensor product. Note that the additional term $-\boldsymbol{\omega} \otimes \boldsymbol{U}$ is added due to the moving mesh. More details about the flux $\boldsymbol{G}$ and the standard ALE-DG methods for conservation laws can be found in [24];

- the operator $:$ is defined as follows

$$A : B := \sum_{1\le i\le n,\ 1\le j\le m} a_{ij} b_{ij}, \tag{2.17}$$

for any two matrices of the same size $A = (a_{ij})$ and $B = (b_{ij}) \in \mathbb{R}^{n\times m}$;
- $\boldsymbol{n}$ is the outer normal vector of $K(t)$ and $\hat{\boldsymbol{G}}$ is the monotone numerical flux.

We use the Harten-Lax-van Leer-contact (HLLC) numerical flux [31] in this paper which is given as follows

$$\hat{\boldsymbol{G}}\left(\boldsymbol{\omega}, \boldsymbol{U}^{int}, \boldsymbol{U}^{ext}, \boldsymbol{n}\right) = \begin{cases} \boldsymbol{G}\left(\boldsymbol{\omega}, \boldsymbol{U}^{int}\right)\cdot \boldsymbol{n}, & \text{if } S^{int} > 0, \\ \boldsymbol{G}^{*,int}, & \text{if } S^{int} \le 0 < S^{M}, \\ \boldsymbol{G}^{*,ext}, & \text{if } S^{M} \le 0 \le S^{ext}, \\ \boldsymbol{G}\left(\boldsymbol{\omega}, \boldsymbol{U}^{ext}\right)\cdot \boldsymbol{n}, & \text{if } S^{ext} < 0, \end{cases} \tag{2.18}$$

where

$$\boldsymbol{U}^{*,int} := \frac{1}{S^{int} - S^{M}} \begin{pmatrix} \left(S^{int} - v^{n,int}\right)\rho^{int} \\ \left(S^{int} - v^{n,int}\right)\boldsymbol{m}^{int} + \left(p^{*} - p^{int}\right)\boldsymbol{n} \\ \left(S^{int} - v^{n,int}\right)E^{int} - p^{int}v^{n,int} + p^{*}S^{M} \end{pmatrix}, \tag{2.19}$$

$$\boldsymbol{U}^{*,ext} := \frac{1}{S^{ext} - S^{M}} \begin{pmatrix} \left(S^{ext} - v^{n,ext}\right)\rho^{ext} \\ \left(S^{ext} - v^{n,ext}\right)\boldsymbol{m}^{ext} + \left(p^{*} - p^{ext}\right)\boldsymbol{n} \\ \left(S^{ext} - v^{n,ext}\right)E^{ext} - p^{ext}v^{n,ext} + p^{*}S^{M} \end{pmatrix}, \tag{2.20}$$

$$\boldsymbol{G}^{*,int} := \begin{pmatrix} S^{M}\rho^{*,int} \\ S^{M}\boldsymbol{m}^{*,int} + p^{*}\boldsymbol{n} \\ S^{M}E^{*,int} + \left(S^{M} + \boldsymbol{\omega}\cdot\boldsymbol{n}\right)p^{*} \end{pmatrix}, \tag{2.21}$$

$$\boldsymbol{G}^{*,ext} := \begin{pmatrix} S^{M}\rho^{*,ext} \\ S^{M}\boldsymbol{m}^{*,ext} + p^{*}\boldsymbol{n} \\ S^{M}E^{*,ext} + \left(S^{M} + \boldsymbol{\omega}\cdot\boldsymbol{n}\right)p^{*} \end{pmatrix}, \tag{2.22}$$

$$\begin{aligned} p^{*} &= \rho^{int}\left(v^{n,int} - S^{int}\right)\left(v^{n,int} - S^{M}\right) + p^{int} \\ &= \rho^{ext}\left(v^{n,ext} - S^{ext}\right)\left(v^{n,ext} - S^{M}\right) + p^{ext}, \end{aligned} \tag{2.23}$$

$$v^{n,int} = \left(\boldsymbol{u}^{int} - \boldsymbol{\omega}\right)\cdot\boldsymbol{n}, \quad v^{n,ext} = \left(\boldsymbol{u}^{ext} - \boldsymbol{\omega}\right)\cdot\boldsymbol{n}, \tag{2.24}$$

and the signal velocities are defined as

$$S^{int} = \min\left(v^{n,int} - c^{int}, v^{n,ext} - c^{ext}\right), \tag{2.25}$$

$$S^{ext} = \max\left(v^{n,int} + c^{int}, v^{n,ext} + c^{ext}\right), \tag{2.26}$$

$$S^{M} = \frac{\rho^{ext}v^{n,ext}\left(S^{ext} - v^{n,ext}\right) - \rho^{int}v^{n,int}\left(S^{int} - v^{n,int}\right) + p^{int} - p^{ext}}{\rho^{ext}\left(S^{ext} - v^{n,ext}\right) - \rho^{int}\left(S^{int} - v^{n,int}\right)}, \tag{2.27}$$

$$c^{int} = \sqrt{\frac{\gamma p^{int}}{\rho^{int}}}, \quad c^{ext} = \sqrt{\frac{\gamma p^{ext}}{\rho^{ext}}}. \tag{2.28}$$

3. The well-balanced ALE-DG methods

In this section, we develop the well-balanced ALE-DG schemes for the Euler equations with gravitation (2.13) on moving meshes.

3.1. Hydrostatic equilibrium states

In this paper, we assume that the desired equilibrium state (1.3) is explicitly given and denote them by $\boldsymbol{U}^{d}$. Two typical examples of the equilibrium state (1.3) are the isothermal [42] or polytropic [21] equilibria outlined below.

Isothermal equilibrium state: For an ideal gas with the isothermal condition, which means that

$$p = \rho RT \quad \text{with } T = T_0 = \text{constant}, \tag{3.1}$$

the equilibrium solution of equations (2.13) is given by

$$\rho = \rho_0 \exp\left(-\frac{\phi}{RT_0}\right), \quad \boldsymbol{u} = 0, \quad p = p_0 \exp\left(-\frac{\phi}{RT_0}\right), \tag{3.2}$$

with $p_0 = \rho_0 RT_0$ and R being the universal gas constant.

Polytropic equilibrium state: If the equilibrium state is set as polytropic gas of the form

$$p = \kappa_0 \rho^{\gamma}, \tag{3.3}$$

one can combine it with the equation (2.13) and obtain the form

$$\rho = \left(\frac{\gamma - 1}{\kappa_0 \gamma}(C - \phi)\right)^{\frac{1}{\gamma - 1}}, \quad \boldsymbol{u} = 0, \quad p = \kappa_0\, \rho^{\gamma}, \tag{3.4}$$

where C and κ_0 are both constants.

3.2. Well-balanced property on the moving mesh

There have been some attempts at the design well-balanced schemes under the framework of ALE methods. In [15], the authors assume a special initial mesh and a Lagrangian moving mesh, which indicates that the mesh does not move at the equilibrium states since the fluid velocity equals zero. If one wishes to achieve the well-balanced property for arbitrarily initial mesh and moving mesh, the situation becomes more complicated. One major difficulty is on the mass conservation as unsuitable treatment of the equation of density ρ may destroy the mass conservation. This is due to the fact that the flux term in the equation of density in (2.16) does not equal zero in the case of an equilibrium state.

In this paper, we would like to address this issue of mass conservation on moving meshes in the setting of the well-balanced framework, and assume that the desired equilibrium state $\boldsymbol{U}^{d}$ is explicitly given. If the initial condition is set as $\boldsymbol{U}^{d}$, we expect the numerical solution of the well-balanced scheme exactly equals a suitable approximation of $\boldsymbol{U}^{d}$, which is independent of the flux and source term of the Euler equations in (2.13). Let us denote such suitable approximation of $\boldsymbol{U}^{d}$ by $\boldsymbol{U}^{e} \in \mathcal{V}_{d}^{k}(t)$. In this case, the well-balanced property is obtained if the flux term and source term balance each other and this leads to

$$\boldsymbol{U}(t) - \boldsymbol{U}^{e}(t) = 0, \tag{3.5}$$

for any time t. The main thing remaining is to define $\boldsymbol{U}^{e}$. There are several different choices for the definitions of $\boldsymbol{U}^{e}$. One can use the L^2 projection to project the desired equilibrium state $\boldsymbol{U}^{d}$ into the time-dependent space $\mathcal{V}_{d}^{k}(t)$, but with such an approach, it is difficult to maintain the positivity of the density and pressure, and the well-balanced property at the same time.

In this work, we introduce a novel approximation of $\boldsymbol{U}^{d}$, which is based on the ALE-DG methods and plays an important role in constructing positivity-preserving schemes. Since $\boldsymbol{U}^{d}$ is the desired hydrostatic equilibrium state, we have

$$\left(\boldsymbol{U}^{d}\right)_{t} = 0, \tag{3.6}$$

at the continuous level. Numerically, we can apply the ALE-DG method to solve this steady state problem (3.6) on the moving meshes, and obtain a numerical approximation of $\boldsymbol{U}^{d}$ on the moving meshes, denoted by $\boldsymbol{U}^{e}$:

$$\frac{\mathrm{d}}{\mathrm{d}t}\int_{K(t)} \boldsymbol{U}^{e}\cdot\boldsymbol{\varphi}\mathrm{d}\boldsymbol{x} = -\int_{K(t)} \left(\boldsymbol{\omega}\otimes\boldsymbol{U}^{e}\right) : \nabla\boldsymbol{\varphi}\mathrm{d}\boldsymbol{x} + \int_{\partial K(t)} \widehat{\boldsymbol{\omega}\otimes\boldsymbol{U}^{e}}\cdot\boldsymbol{\varphi}\mathrm{d}s, \tag{3.7}$$

where $\widehat{\boldsymbol{\omega}\otimes\boldsymbol{U}^{e}}$ is the numerical flux of $\boldsymbol{\omega}\otimes\boldsymbol{U}^{e}$ which depends on the specific well-balanced methods to be used and will be defined later. The initial condition of $\boldsymbol{U}^{e}$ is set as the L^2 projection of $\boldsymbol{U}^{d}$:

$$\boldsymbol{U}^{e}(x, t=0) = \mathcal{P}\boldsymbol{U}^{d}(x, t=0), \tag{3.8}$$

where $\mathcal{P}$ stands for the standard element-wise L^2 projection. Again, we emphasize that the objective of the proposed well-balanced will be to preserve $\boldsymbol{U}^{e}(t)$ (an approximation of $\boldsymbol{U}^{d}(t)$) at all time steps.

3.3. The semi-discrete well-balanced ALE-DG scheme

In this subsection, two well-balanced schemes will be introduced. The first one is based on the hydrostatic reconstruction [1] and can be viewed as an extension of the well-balanced methods studied in [29,49] to the moving meshes. The second one is based on a special source term reformulation and the modified HLLC flux as studied in [38]. In the first approach, the Lax-Friedrichs numerical flux in [49] is replaced by the HLLC flux in this paper, as better results in the accuracy test on the moving meshes have been observed numerically.

3.3.1. Well-balanced scheme based on hydrostatic reconstruction

We start by presenting the first approach to obtaining well-balanced methods. We adopt the well-balanced idea in [49] by modifying the cell boundary values and applying the hydrostatic reconstruction idea. Since the ALE-DG methods are designed based on the moving meshes, the main challenge is to introduce the well-balanced numerical flux involving the grid velocity $\boldsymbol{\omega}$ and the updated definition of $\boldsymbol{U}^e$ based on the ALE-DG scheme (3.7).

We begin with the definitions of modified cell boundary values. At each time step t^n, let us decompose the numerical solution $\boldsymbol{U}$ into two parts: one is the equilibrium part $\boldsymbol{U}^e$ defined in (3.7) and the other is the fluctuation part

$$\boldsymbol{U}^f := \boldsymbol{U} - \boldsymbol{U}^e. \tag{3.9}$$

The modified cell boundary values are given by

$$\begin{aligned}
&\boldsymbol{U}^{*,int_{K(t)}} = \boldsymbol{U}^{\tilde{e},int_{K(t)}} + \boldsymbol{U}^{f,int_{K(t)}}, && \boldsymbol{U}^{*,ext_{K(t)}} = \boldsymbol{U}^{\tilde{e},ext_{K(t)}} + \boldsymbol{U}^{f,ext_{K(t)}},\\
&\rho^{b,int_{K(t)}} = \max\left(0, \rho^{*,int_{K(t)}}\right), && \rho^{b,ext_{K(t)}} = \max\left(0, \rho^{*,ext_{K(t)}}\right),\\
&\boldsymbol{u}^{b,int_{K(t)}} = \boldsymbol{u}^{int_{K(t)}}, && \boldsymbol{u}^{b,ext_{K(t)}} = \boldsymbol{u}^{ext_{K(t)}},\\
&p^{b,int_{K(t)}} = \max\left(0, p^{*,int_{K(t)}}\right), && p^{b,ext_{K(t)}} = \max\left(0, p^{*,ext_{K(t)}}\right),
\end{aligned} \tag{3.10}$$

where

$$\boldsymbol{U}^{\tilde{e}} = \tilde{\mathcal{P}}^{k+1}\boldsymbol{U}^d \in \boldsymbol{\mathcal{V}}_d^{k+1}(t), \tag{3.11}$$

is the projection of $\boldsymbol{U}^d$ onto $K(t)$, and $\tilde{\mathcal{P}}$ denotes the continuous finite element projection introduced in [6]. The motivation for introducing the projection of degree $k+1$ is to provide a more accurate source term approximation and to maintain the continuity at the cell boundaries, as explained in [49]. We refer [6, Figs. 3.1, 3.3–3.5] for examples of 2D projection on triangular cell. One nice property of $\boldsymbol{U}^{\tilde{e}}$ is that it is continuous at the cell boundaries, i.e.

$$\boldsymbol{U}^{\tilde{e},int_{K(t)}} = \boldsymbol{U}^{\tilde{e},ext_{K(t)}}. \tag{3.12}$$

If the purpose is to maintain only the well-balanced property, it is unnecessary to introduce such projection $\tilde{\mathcal{P}}$ since one can simply set $\boldsymbol{U}^{\tilde{e}} = \boldsymbol{U}^d$. If we want to have the positivity-preserving property at the same time, such projection will be used in the source term approximation (3.13) and plays an important role in the proof of the positivity-preserving property.

Following the approximation of the source term $\int_{K(t)} \boldsymbol{S}(\boldsymbol{U}, \nabla\phi)\cdot\boldsymbol{\varphi}\mathrm{d}\boldsymbol{x}$ in [49], we separate the source term into two terms involving $\boldsymbol{U}^e$ and $\boldsymbol{U}^f$ respectively, and approximate them by

$$\begin{aligned}
S^h_{K(t)} = &\int_{K(t)} \boldsymbol{S}\left(\boldsymbol{U}^f, -\frac{\nabla p^{\tilde{e}}}{\rho^e}\right)\cdot\boldsymbol{\varphi}\mathrm{d}\boldsymbol{x} - \int_{K(t)} \boldsymbol{F}(\boldsymbol{U}^e) : \nabla\boldsymbol{\varphi}\mathrm{d}\boldsymbol{x}\\
&+ \int_{\partial K(t)} \left(\boldsymbol{F}\left(\boldsymbol{U}^{\tilde{e}}\right)\cdot\boldsymbol{n}\right)\cdot\boldsymbol{\varphi}^{int_{K(t)}}\mathrm{d}\boldsymbol{s}.
\end{aligned} \tag{3.13}$$

Note that although the form of $S^h_{K(t)}$ is the same as that in [49], it involves different $\boldsymbol{U}^e$ and $\boldsymbol{U}^{\tilde{e}}$, now defined over the moving meshes.

The proposed well-balanced ALE-DG scheme based on the hydrostatic reconstruction is given by: find $\boldsymbol{U} \in \boldsymbol{\mathcal{V}}_d^k(t)$, such that

$$\frac{\mathrm{d}}{\mathrm{d}t}\int_{K(t)} \boldsymbol{U}\cdot\boldsymbol{\varphi}\mathrm{d}\boldsymbol{x} = \boldsymbol{\mathcal{L}}^h_K(\boldsymbol{\omega}, \boldsymbol{U}, \boldsymbol{\varphi}, t), \tag{3.14}$$

holds for any $\boldsymbol{\varphi} \in \boldsymbol{\mathcal{V}}_d^k(t)$, where the spatial operator is given by

$$\begin{aligned}
&\boldsymbol{\mathcal{L}}^h_K(\boldsymbol{\omega}, \boldsymbol{U}, \boldsymbol{\varphi}, t)\\
&= \int_{K(t)} \boldsymbol{G}(\boldsymbol{\omega}, \boldsymbol{U}) : \nabla\boldsymbol{\varphi}\mathrm{d}\boldsymbol{x} - \int_{\partial K(t)} \hat{\boldsymbol{G}}\left(\boldsymbol{\omega}, \boldsymbol{U}^{b,int_{K(t)}}, \boldsymbol{U}^{b,ext_{K(t)}}, \boldsymbol{n}\right)\cdot\boldsymbol{\varphi}\mathrm{d}\boldsymbol{s} + S^h_{K(t)},
\end{aligned} \tag{3.15}$$

with $S^h_{K(t)}$ defined in (3.13), $\hat{\boldsymbol{G}}$ defined in (2.18) and $\boldsymbol{U}^{b,int_{K(t)}}, \boldsymbol{U}^{b,ext_{K(t)}}$ defined in (3.10). The last thing is to define the corresponding numerical flux $\widehat{\boldsymbol{\omega}\otimes\boldsymbol{U}^e}$ in (3.7):

$$\widehat{\boldsymbol{\omega}\otimes\boldsymbol{U}^e} := (\boldsymbol{\omega}\otimes\boldsymbol{U}^{\tilde{e}})\cdot\boldsymbol{n}, \tag{3.16}$$

where $\boldsymbol{U}^{\tilde{e}}$ is defined in (3.11).

Next, we introduce the following lemma, demonstrating the well-balancedness of the semi-discrete scheme (3.14).

Lemma 3.1. *If the numerical solution reaches the equilibrium state, i.e. $\boldsymbol{U} = \boldsymbol{U}^e$, the spatial operator in the semi-discrete ALE-DG scheme (3.14) reduces to*

$$\boldsymbol{\mathcal{L}}^h_K(\boldsymbol{\omega}, \boldsymbol{U}, \boldsymbol{\varphi}, t) = \int_{\partial K(t)} \widehat{\boldsymbol{\omega}\otimes\boldsymbol{U}^e}\cdot\boldsymbol{\varphi}\mathrm{d}\boldsymbol{s} - \int_{K(t)} (\boldsymbol{\omega}\otimes\boldsymbol{U}^e) : \nabla\boldsymbol{\varphi}\mathrm{d}\boldsymbol{x},$$

which leads to the well-balanced property of spatial discretization.

Proof. We first claim that $\boldsymbol{U}^{b,int_{K(t)}} = \boldsymbol{U}^{b,ext_{K(t)}} = \boldsymbol{U}^{\tilde{e},int_{K(t)}} = \boldsymbol{U}^{\tilde{e},ext_{K(t)}}$ in (3.10), following the fact that $\boldsymbol{U}^f = \boldsymbol{U} - \boldsymbol{U}^e = 0$ and (3.12). The consistency property of the HLLC flux leads to

$$\begin{aligned}
\hat{\boldsymbol{G}}\left(\boldsymbol{\omega}, \boldsymbol{U}^{b,int_{K(t)}}, \boldsymbol{U}^{b,ext_{K(t)}}, \boldsymbol{n}\right) &= \boldsymbol{G}\left(\boldsymbol{\omega}, \boldsymbol{U}^{b,int_{K(t)}}\right)\cdot\boldsymbol{n}\\
&= \left(\boldsymbol{F}\left(\boldsymbol{U}^{\tilde{e},int_{K(t)}}\right) - \boldsymbol{\omega}\otimes\boldsymbol{U}^{\tilde{e},int_{K(t)}}\right)\cdot\boldsymbol{n}.
\end{aligned}$$

Using the assumption $\boldsymbol{U} = \boldsymbol{U}^e$ and the definition of source term (3.13), we have

$$\begin{aligned}
\boldsymbol{\mathcal{L}}^h_K(\boldsymbol{\omega}, \boldsymbol{U}, \boldsymbol{\varphi}, t) = &\int_{K(t)} \boldsymbol{G}(\boldsymbol{\omega}, \boldsymbol{U}^e) : \nabla\boldsymbol{\varphi}\mathrm{d}\boldsymbol{x}\\
&- \int_{\partial K(t)} \left(\left(\boldsymbol{F}(\boldsymbol{U}^{\tilde{e},int_{K(t)}}) - \boldsymbol{\omega}\otimes\boldsymbol{U}^{\tilde{e},int_{K(t)}}\right)\cdot\boldsymbol{n}\right)\cdot\boldsymbol{\varphi}\mathrm{d}\boldsymbol{s}\\
&- \int_{K(t)} \boldsymbol{F}(\boldsymbol{U}^e) : \nabla\boldsymbol{\varphi}\mathrm{d}\boldsymbol{x} + \int_{\partial K(t)} \left(\boldsymbol{F}\left(\boldsymbol{U}^{\tilde{e},int_{K(t)}}\right)\cdot\boldsymbol{n}\right)\cdot\boldsymbol{\varphi}^{int_{K(t)}}\mathrm{d}\boldsymbol{s}\\
= &\int_{\partial K(t)} \left(\left(\boldsymbol{\omega}\otimes\boldsymbol{U}^{\tilde{e},int_{K(t)}}\right)\cdot\boldsymbol{n}\right)\cdot\boldsymbol{\varphi}\mathrm{d}\boldsymbol{s} - \int_{K(t)} (\boldsymbol{\omega}\otimes\boldsymbol{U}^e) : \nabla\boldsymbol{\varphi}\mathrm{d}\boldsymbol{x}\\
= &\int_{\partial K(t)} \widehat{\boldsymbol{\omega}\otimes\boldsymbol{U}^e}\cdot\boldsymbol{\varphi}\mathrm{d}\boldsymbol{s} - \int_{K(t)} (\boldsymbol{\omega}\otimes\boldsymbol{U}^e) : \nabla\boldsymbol{\varphi}\mathrm{d}\boldsymbol{x},
\end{aligned}$$

where the last equality follows from (3.16). This finishes the proof. □

3.3.2. Well-balanced scheme based on a special source term approximation

A different approach to obtaining a well-balanced scheme will be discussed in this section. This is inspired by the recent work in [38], in which a positivity-preserving well-balanced DG scheme has been proposed on the static mesh. Compared with the work in [38], the definition of $\boldsymbol{U}^e$ will be different and the numerical flux now involves the grid velocity $\boldsymbol{\omega}$, again due to the moving meshes, while the form of the source term approximation and the modified cell boundary values are the same.

We begin with presenting the modified cell boundary values in [38]:

$$\boldsymbol{U}^{\check{b},int_{K(t)}} = \frac{p^c}{p^{e,int_{K(t)}}}\boldsymbol{U}^{int_{K(t)}}, \quad \boldsymbol{U}^{\check{b},ext_{K(t)}} = \frac{p^c}{p^{e,ext_{K(t)}}}\boldsymbol{U}^{ext_{K(t)}}, \tag{3.17}$$

where p^c is defined as the average of cell boundary values

$$p^c = \frac{p^{e,int_{K(t)}} + p^{e,ext_{K(t)}}}{2}. \tag{3.18}$$

In [38], a novel source term approximation based on the source term reformulation idea in [41] has been introduced in one dimension and extended to two dimensions on rectangular meshes. A similar approximation will be utilized here, and extended to moving meshes, including two-dimensional triangular moving meshes. Let us denote the approximation of $\int_{K(t)} \boldsymbol{S}(\boldsymbol{U}, \nabla\phi)\cdot\boldsymbol{\varphi}\mathrm{d}\boldsymbol{x}$ by $S^s_{K(t)}$. We use $\boldsymbol{S}^{[j]}$ denotes the j-th component of $\boldsymbol{S}$, and similarly for $\boldsymbol{\varphi}$. The source term approximations are given by

$$\begin{aligned}
&\int_{K(t)} \boldsymbol{S}^{[1]}(\boldsymbol{U}, \nabla\phi)\boldsymbol{\varphi}^{[1]}\mathrm{d}\boldsymbol{x} = 0 =: \langle \boldsymbol{S}^{[1]}, \boldsymbol{\varphi}^{[1]}\rangle,\\
&\int_{K(t)} \boldsymbol{S}^{[2]}(\boldsymbol{U}, \nabla\phi)\cdot\boldsymbol{\varphi}^{[2]}\mathrm{d}\boldsymbol{x}\\
&\quad\approx \int_{K(t)} \rho\frac{\nabla p^e}{\rho^e}\cdot\boldsymbol{\varphi}^{[2]}\mathrm{d}\boldsymbol{x} + \frac{\bar{\rho}}{\bar{\rho}^e}\int_{\partial K(t)} \frac{p^{e,ext_{K(t)}} - p^{e,int_{K(t)}}}{2}\boldsymbol{n}\cdot\boldsymbol{\varphi}^{[2]}\mathrm{d}s\\
&\quad=: \langle \boldsymbol{S}^{[2]}, \boldsymbol{\varphi}^{[2]}\rangle,\\
&\int_{K(t)} \boldsymbol{S}^{[3]}(\boldsymbol{U}, \nabla\phi)\boldsymbol{\varphi}^{[3]}\mathrm{d}\boldsymbol{x}\\
&\quad\approx \int_{K(t)} \boldsymbol{m}\cdot\frac{\nabla p^e}{\rho^e}\boldsymbol{\varphi}^{[3]}\mathrm{d}\boldsymbol{x} + \frac{\bar{\boldsymbol{m}}}{\bar{\rho}^e}\cdot\int_{\partial K(t)} \frac{p^{e,ext_{K(t)}} - p^{e,int_{K(t)}}}{2}\boldsymbol{n}\boldsymbol{\varphi}^{[3]}\mathrm{d}s\\
&\quad=: \langle \boldsymbol{S}^{[3]}, \boldsymbol{\varphi}^{[3]}\rangle,\\
&S^s_{K(t)} = \langle \boldsymbol{S}^{[1]}, \boldsymbol{\varphi}^{[1]}\rangle + \langle \boldsymbol{S}^{[2]}, \boldsymbol{\varphi}^{[2]}\rangle + \langle \boldsymbol{S}^{[3]}, \boldsymbol{\varphi}^{[3]}\rangle.
\end{aligned} \tag{3.19}$$

Here $\bar{\boldsymbol{U}}$, $\bar{\boldsymbol{U}}^e$ are the cell average of $\boldsymbol{U}$, $\boldsymbol{U}^e$ respectively. More details about this approximation can be found in [38]. Note that the formulation in (3.19) is slightly different from that in [38], as an additional integration-by-parts procedure is applied here to simplify the notations. We note that sufficient integration accuracy in (3.19) for polynomials of degree $2k-1$ on $K(t)$ and $2k$ on $\partial K(t)$ is needed to maintain the well-balanced property, since we will use integration by parts on the polynomial integration in the proof of well-balanced property and this only holds with exact integration of these polynomials. The details will be shown in Lemma 3.3.

The well-balanced ALE-DG scheme based on a special source term approximation is given by: find $\boldsymbol{U}\in\mathcal{V}_d^k(t)$, such that

$$\frac{\mathrm{d}}{\mathrm{d}t}\int_{K(t)} \boldsymbol{U}\cdot\boldsymbol{\varphi}\mathrm{d}\boldsymbol{x} = \mathcal{L}^s_K(\boldsymbol{\omega}, \boldsymbol{U}, \boldsymbol{\varphi}, t), \tag{3.20}$$

holds for any $\boldsymbol{\varphi}\in\mathcal{V}_d^k(t)$, where the spatial operator is given by

$$\begin{aligned}
&\mathcal{L}^s_K(\boldsymbol{\omega}, \boldsymbol{U}, \boldsymbol{\varphi}, t)\\
&= \int_{K(t)} \boldsymbol{G}(\boldsymbol{\omega}, \boldsymbol{U}) : \nabla\boldsymbol{\varphi}\mathrm{d}\boldsymbol{x} - \int_{\partial K(t)} \hat{\boldsymbol{G}}\left(\boldsymbol{\omega}, \boldsymbol{U}^{\tilde{b},int_{K(t)}}, \boldsymbol{U}^{\tilde{b},ext_{K(t)}}, \boldsymbol{n}\right)\cdot\boldsymbol{\varphi}\mathrm{d}s + S^s_{K(t)},
\end{aligned} \tag{3.21}$$

with $S^s_{K(t)}$ defined in (3.19), $\hat{\boldsymbol{G}}$ defined in (2.18) and $\boldsymbol{U}^{\tilde{b},int}, \boldsymbol{U}^{\tilde{b},ext}$ defined in (3.17). The definition of the corresponding numerical flux $\widehat{\boldsymbol{\omega}\otimes\boldsymbol{U}^e}$ in the method (3.7) takes the form

$$\widehat{\boldsymbol{\omega}\otimes\boldsymbol{U}^e} := \begin{cases} \frac{p^c}{p^{e,int_{K(t)}}}(\boldsymbol{\omega}\otimes\boldsymbol{U}^{e,int_{K(t)}})\cdot\boldsymbol{n}, & \text{if } \boldsymbol{\omega}\cdot\boldsymbol{n} < 0,\\ \frac{p^c}{p^{e,ext_{K(t)}}}(\boldsymbol{\omega}\otimes\boldsymbol{U}^{e,ext_{K(t)}})\cdot\boldsymbol{n}, & \text{if } \boldsymbol{\omega}\cdot\boldsymbol{n} > 0. \end{cases} \tag{3.22}$$

Next, we present the following lemmas on the well-balancedness of the semi-discrete scheme (3.20).

Lemma 3.2. *For the pair of $(\boldsymbol{U}^{int}, \boldsymbol{U}^{ext})$ with $\boldsymbol{m}^{int} = \boldsymbol{m}^{ext} = 0$ and $p^{int} = p^{ext} = p$, the HLLC flux (2.18) satisfies*

$$\hat{\boldsymbol{G}}(\boldsymbol{\omega}, \boldsymbol{U}^{int}, \boldsymbol{U}^{ext}, \boldsymbol{n}) = \begin{cases} \boldsymbol{G}(\boldsymbol{\omega}, \boldsymbol{U}^{int})\cdot\boldsymbol{n}, & \text{if } \boldsymbol{\omega}\cdot\boldsymbol{n} < 0,\\ \boldsymbol{G}(\boldsymbol{\omega}, \boldsymbol{U}^{ext})\cdot\boldsymbol{n}, & \text{if } \boldsymbol{\omega}\cdot\boldsymbol{n} > 0. \end{cases} \tag{3.23}$$

Proof. First, we introduce the notations $\omega^n = \boldsymbol{\omega}\cdot\boldsymbol{n}$, $c_m = \max\left(c^{int}, c^{ext}\right)$. By using the assumption $\boldsymbol{m}^{int} = \boldsymbol{m}^{ext} = 0$, the signal velocities in (2.25)–(2.27) can be simplified to

$$S^{int} = -c_m - \omega^n, \quad S^{ext} = c_m - \omega^n, \quad S^M = -\omega^n. \tag{3.24}$$

Note that $S^M = v^{n,int} = v^{n,ext} = -\omega^n$ in (2.24) and (2.27), which leads to $p^* = p = p^{int} = p^{ext}$ in (2.23). One can then simplify the intermediate states in (2.19) and (2.20) as

$$\boldsymbol{U}^{*,int} = \boldsymbol{U}^{int}, \quad \boldsymbol{U}^{*,ext} = \boldsymbol{U}^{ext},$$

and the corresponding numerical flux in (2.21) and (2.22) as

$$\boldsymbol{G}^{*,int} = \boldsymbol{G}\left(\boldsymbol{\omega}, \boldsymbol{U}^{int}\right)\cdot\boldsymbol{n}, \quad \boldsymbol{G}^{*,ext} = \boldsymbol{G}\left(\boldsymbol{\omega}, \boldsymbol{U}^{ext}\right)\cdot\boldsymbol{n}.$$

Combining this with the signal velocities, one can conclude (3.23), and this finishes the proof. □

Lemma 3.3. *If the numerical solution reaches the equilibrium state, i.e. $\boldsymbol{U} = \boldsymbol{U}^e$, the spatial operator in the semi-discrete ALE-DG scheme (3.20) reduces to*

$$\mathcal{L}^s_K(\boldsymbol{\omega}, \boldsymbol{U}, \boldsymbol{\varphi}, t) = \int_{\partial K(t)} \widehat{\boldsymbol{\omega}\otimes\boldsymbol{U}^e}\cdot\boldsymbol{\varphi}\mathrm{d}s - \int_{K(t)} (\boldsymbol{\omega}\otimes\boldsymbol{U}^e) : \nabla\boldsymbol{\varphi}\mathrm{d}\boldsymbol{x},$$

which leads to the well-balanced property of the spatial discretization.

Proof. We first claim that $p^{\tilde{b},int_{K(t)}} = p^c$ in (3.17), due to the fact that $\boldsymbol{U} = \boldsymbol{U}^e$ and

$$p^{\tilde{b},int_{K(t)}} = \frac{p^c}{p^{e,int_{K(t)}}} p^{int_{K(t)}} = p^c.$$

Similarly, we have $p^{\tilde{b},ext_{K(t)}} = p^c$ and $p^{\tilde{b},int_{K(t)}} = p^{\tilde{b},ext_{K(t)}}$. Utilizing the property of HLLC flux in Lemma 3.2 yields

$$\hat{\boldsymbol{G}}\left(\boldsymbol{\omega}, \boldsymbol{U}^{\tilde{b},int_{K(t)}}, \boldsymbol{U}^{\tilde{b},ext_{K(t)}}, \boldsymbol{n}\right) = \begin{cases} \boldsymbol{G}\left(\boldsymbol{\omega}, \boldsymbol{U}^{\tilde{b},int_{K(t)}}\right)\cdot\boldsymbol{n}, & \text{if } \boldsymbol{\omega}\cdot\boldsymbol{n} < 0,\\ \boldsymbol{G}\left(\boldsymbol{\omega}, \boldsymbol{U}^{\tilde{b},ext_{K(t)}}\right)\cdot\boldsymbol{n}, & \text{if } \boldsymbol{\omega}\cdot\boldsymbol{n} > 0. \end{cases} \tag{3.25}$$

For the source term approximation $S^s_{K(t)}$, we use the assumption $\rho = \rho^e$, $\boldsymbol{m} = \boldsymbol{m}^e = 0$ and the definition (3.19) to conclude that

$$\begin{aligned}
&\langle \boldsymbol{S}^{[1]}, \boldsymbol{\varphi}^{[1]}\rangle = \langle \boldsymbol{S}^{[3]}, \boldsymbol{\varphi}^{[3]}\rangle = 0,\\
&S^s_{K(t)} = \langle \boldsymbol{S}^{[2]}, \boldsymbol{\varphi}^{[2]}\rangle = \int_{K(t)} \nabla p^e\cdot\boldsymbol{\varphi}^{[2]}\mathrm{d}\boldsymbol{x} + \int_{\partial K(t)} \frac{p^{e,ext_{K(t)}} - p^{e,int_{K(t)}}}{2}\boldsymbol{n}\cdot\boldsymbol{\varphi}^{[2]}\mathrm{d}s\\
&\qquad= -\int_{K(t)} p^e\, I : \nabla\boldsymbol{\varphi}^{[2]}\mathrm{d}\boldsymbol{x} + \int_{\partial K(t)} p^c\boldsymbol{n}\cdot\boldsymbol{\varphi}^{[2]}\mathrm{d}s,
\end{aligned} \tag{3.26}$$

where the last equality follows from integration by part (which holds with sufficient integration accuracy) and the definition of p^e in (3.18). Based on the assumptions $\boldsymbol{U} = \boldsymbol{U}^e$, $\boldsymbol{m} = 0$, we have

$$\boldsymbol{G}(\boldsymbol{\omega}, \boldsymbol{U}) = \begin{pmatrix} 0\\ pI\\ 0 \end{pmatrix} - \boldsymbol{\omega}\otimes\boldsymbol{U},$$

and can conclude that

$$\begin{aligned}
&\mathcal{L}^s_K(\boldsymbol{\omega}, \boldsymbol{U}, \boldsymbol{\varphi}, t)\\
&= \int_{K(t)} \boldsymbol{G}(\boldsymbol{\omega}, \boldsymbol{U}) : \nabla\boldsymbol{\varphi}\mathrm{d}\boldsymbol{x} - \int_{\partial K(t)} \hat{\boldsymbol{G}}\left(\boldsymbol{\omega}, \boldsymbol{U}^{\tilde{b},int_{K(t)}}, \boldsymbol{U}^{\tilde{b},ext_{K(t)}}, \boldsymbol{n}\right)\cdot\boldsymbol{\varphi}\mathrm{d}s + S^s_{K(t)}\\
&= \int_{K(t)} \boldsymbol{G}(\boldsymbol{\omega}, \boldsymbol{U}) : \nabla\boldsymbol{\varphi}\mathrm{d}\boldsymbol{x} - \int_{\partial K(t)} p^c\boldsymbol{n}\cdot\boldsymbol{\varphi}^{[2]} - \widehat{\boldsymbol{\omega}\otimes\boldsymbol{U}^e}\cdot\boldsymbol{\varphi}\mathrm{d}s
\end{aligned}$$

$$+\left(\int_{\partial K(t)} p^c \boldsymbol{n}\cdot\boldsymbol{\varphi}^{[2]}\mathrm{d}s-\int_{K(t)} p^e\, I:\nabla\boldsymbol{\varphi}^{[2]}\mathrm{d}\boldsymbol{x}\right)$$
$$=\int_{\partial K(t)}\widehat{\boldsymbol{\omega}\otimes\boldsymbol{U}^e}\cdot\boldsymbol{\varphi}\mathrm{d}s-\int_{K(t)}(\boldsymbol{\omega}\otimes\boldsymbol{U}^e):\nabla\boldsymbol{\varphi}\mathrm{d}\boldsymbol{x},$$

where the second equality follows from the combination of (3.22), (3.25), (3.26), the definition of $\boldsymbol{U}^{\tilde{b}}$ in (3.17) and the assumptions $\boldsymbol{U}=\boldsymbol{U}^e$, $\boldsymbol{m}=0$. □

3.4. Time discretization and well-balanced property

We use the standard TVD-RK time discretization with slight modifications introduced in [14] in the multi-dimensional case in this paper. For the ALE-DG methods, the TVD-RK time discretization may destroy the well-balanced property because the spatial discretization $\mathcal{L}_K^{h/s}$ applied to the equilibrium states do not equal 0, as indicated in Lemma 3.1 and Lemma 3.3. Therefore, we would apply the same time discretization for the approximation $\boldsymbol{U}^e$ to ensure $\boldsymbol{U}=\boldsymbol{U}^e$ at each time step.

We start with presenting the standard s-stage TVD-RK time discretization: for $i=1,\cdots,s$,

$$\int_{K^{n,i}}\boldsymbol{U}^{n,i}\cdot\boldsymbol{\varphi}^{n,i}\mathrm{d}\boldsymbol{x}$$
$$=\sum_{j=0}^{i-1}\left(\alpha_{ij}\int_{K^{n,j}}\boldsymbol{U}^{n,j}\cdot\boldsymbol{\varphi}^{n,j}\mathrm{d}\boldsymbol{x}+\beta_{ij}\Delta t\mathcal{L}_{K^{n,j}}\left(\boldsymbol{\omega}^{n,j},\boldsymbol{U}^{n,j},\boldsymbol{\varphi}^{n,j},t^{n,j}\right)\right),$$

where $t^{n,0}=t^n$, $t^{n,s}=t^{n+1}$ and $\boldsymbol{\varphi}^{n,i}$, for $i=1,\cdots,s$ are the corresponding test functions at time $t^{n,i}$ as defined in (2.11). The constants $\{\alpha_{ij}\}$ and $\{\beta_{ij}\}$ refer to the coefficients of the TVD-RK methods, which can be found in [17]. For example, the Euler forward time discretization corresponds to the case $s=1,\alpha_{10}=1,\beta_{10}=1$, i.e.,

$$\int_{K^{n+1}}\boldsymbol{U}^{n+1}\cdot\boldsymbol{\varphi}^{n+1}\mathrm{d}\boldsymbol{x}=\int_{K^n}\boldsymbol{U}^n\cdot\boldsymbol{\varphi}^n\mathrm{d}\boldsymbol{x}+\Delta t\mathcal{L}_{K^n}\left(\boldsymbol{\omega}^n,\boldsymbol{U}^n,\boldsymbol{\varphi}^n,t^n\right).$$

Next, we introduce the approximation of the cell volume $\Delta_{K^{n,i}}$, denoted by $J_{K^{n,i}}$, for $i=1,\cdots,s$, which is defined by employing the TVD-RK methods:

$$J_{K^{n,i}}=\sum_{j=0}^{i-1}\left(\alpha_{ij}+\beta_{ij}\Delta t\nabla_{\boldsymbol{x}^{n,j}}\cdot\boldsymbol{\omega}^{n,j}\right)J_{K^{n,j}},\tag{3.27}$$

where $J_{K^{n,0}}=\Delta_{K^n}$.

The modified s-stage TVD-RK time discretization [14] to be used in this paper takes the form

$$\frac{J_{K^{n,i}}}{\Delta_{K^{n,i}}}\int_{K^{n,i}}\boldsymbol{U}^{n,i}\cdot\boldsymbol{\varphi}^{n,i}\mathrm{d}\boldsymbol{x}$$
$$=\sum_{j=0}^{i-1}\frac{J_{K^{n,j}}}{\Delta_{K^{n,j}}}\left(\alpha_{ij}\int_{K^{n,j}}\boldsymbol{U}^{n,j}\cdot\boldsymbol{\varphi}^{n,j}\mathrm{d}\boldsymbol{x}+\beta_{ij}\Delta t\mathcal{L}_{K^{n,j}}\left(\boldsymbol{\omega}^{n,j},\boldsymbol{U}^{n,j},\boldsymbol{\varphi}^{n,j},t^{n,j}\right)\right),\tag{3.28}$$

for $i=1,\cdots,s$, with the main difference being the additional coefficients $\frac{J_{K^{n,i}}}{\Delta_{K^{n,i}}}$. $\mathcal{L}_{K^{n,j}}$ in (3.28) can be replaced by $\mathcal{L}^h_{K^{n,j}}$ in (3.14) or $\mathcal{L}^s_{K^{n,j}}$ in (3.20), leading to two fully-discrete well-balanced ALE-DG schemes.

The GCL is an important property to keep high order accuracy and well-balanced property for the grid deformation method. We introduce the GCL briefly and refer to [24] for details. If a method satisfies the GCL, it can preserve the constant states. Both proposed schemes satisfy the GCL property, and we provide brief proof for the 2D case. First, if a constant state satisfies our model (1.1), the gravitational potential ϕ should also be a constant. In this case, we set the equilibrium state $\boldsymbol{U}^d$ as the same constant state. We have the reference equilibrium states $\boldsymbol{U}^e=\boldsymbol{U}^{\tilde{e}}=\boldsymbol{U}^d=\boldsymbol{U}$, all being constants, and $\widehat{\boldsymbol{\omega}\otimes\boldsymbol{U}^e}=\boldsymbol{\omega}\otimes\boldsymbol{U}$ on the cell boundary. Following Lemmas 3.1 and 3.3, (3.28) reduces to

$$\frac{J_{K^{n,i}}}{\Delta_{K^{n,i}}}\int_{K^{n,i}}\boldsymbol{U}^{n,i}\cdot\boldsymbol{\varphi}^{n,i}\mathrm{d}\boldsymbol{x}$$
$$=\sum_{j=0}^{i-1}\frac{J_{K^{n,j}}}{\Delta_{K^{n,j}}}\left(\alpha_{ij}\int_{K^{n,j}}\boldsymbol{U}^{n,j}\cdot\boldsymbol{\varphi}^{n,j}\mathrm{d}\boldsymbol{x}+\beta_{ij}\Delta t\left(\int_{K^{n,j}}\left(\nabla\cdot\left(\boldsymbol{\omega}^{n,j}\otimes\boldsymbol{U}^{n,j}\right)\right)\cdot\boldsymbol{\varphi}^{n,j}\mathrm{d}\boldsymbol{x}\right)\right)$$
$$=\sum_{j=0}^{i-1}\frac{J_{K^{n,j}}}{\Delta_{K^{n,j}}}\left(\alpha_{ij}\int_{K^{n,j}}\boldsymbol{U}^{n,j}\cdot\boldsymbol{\varphi}^{n,j}\mathrm{d}\boldsymbol{x}+\beta_{ij}\Delta t\left(\int_{K^{n,j}}\left(\nabla\cdot\boldsymbol{\omega}^{n,j}\right)\boldsymbol{U}^{n,j}\cdot\boldsymbol{\varphi}^{n,j}\mathrm{d}\boldsymbol{x}\right)\right),$$

where the first equality follows from the results above and the integral by part, and the second equality holds as $\boldsymbol{U}$ is a constant state. By setting the test function $\boldsymbol{\varphi}=1$ and using equation (3.27), we can easily prove $\boldsymbol{U}^{n,j}=\boldsymbol{U}^n$ for all j, i.e., $\boldsymbol{U}^{n+1}$ is still a constant state. From this, we can also observe why we need to slightly modify the Runge-Kutta time discretization with the term (3.27). We refer to [14] for more discussion on this term.

We will prove that the fully discrete well-balanced ALE-DG scheme (3.28), when coupled with the modified TVD-RK methods, preserves the equilibrium state at a discrete level. For ease of presentation, we will demonstrate the well-balanced property of the fully discrete ALE-DG scheme with the modified Euler forward time discretization:

$$\frac{\left(1+\Delta t\nabla_{\boldsymbol{x}^n}\cdot\boldsymbol{\omega}^n\right)\Delta_{K^n}}{\Delta_{K^{n+1}}}\int_{K^{n+1}}\boldsymbol{U}^{n+1}\cdot\boldsymbol{\varphi}^{n+1}\mathrm{d}\boldsymbol{x}$$
$$=\int_{K^n}\boldsymbol{U}^n\cdot\boldsymbol{\varphi}^n\mathrm{d}\boldsymbol{x}+\Delta t\mathcal{L}_{K^n}\left(\boldsymbol{\omega}^n,\boldsymbol{U}^n,\boldsymbol{\varphi}^n,t^n\right),\tag{3.29}$$

where $\boldsymbol{\varphi}^{n+1}$ and $\boldsymbol{\varphi}^n$ are the corresponding test functions (2.11) at time t^{n+1} and t^n respectively. The same proof can be easily extended to general TVD-RK methods.

Proposition 3.4. *The fully discrete schemes described in (3.29), with $\mathcal{L}_{K^{n,j}}$ replaced by $\mathcal{L}^h_{K^{n,j}}$ in (3.14) or $\mathcal{L}^s_{K^{n,j}}$ in (3.20), maintain the equilibrium state exactly, which means that $\boldsymbol{U}^n=\boldsymbol{U}^{e,n}$ for all time level t^n.*

Proof. We will use induction to prove the result of $\boldsymbol{U}^n=\boldsymbol{U}^{e,n}$, $\forall n\in\mathbb{N}$.

Basic Step: Suppose that the exact solution $\boldsymbol{U}_{ex}$ equals the desired hydrostatic equilibrium state $\boldsymbol{U}^d$. Since the initial condition $\boldsymbol{U}^0$ and $\boldsymbol{U}^{e,0}$ are both the L^2 projection of $\boldsymbol{U}^d$, we have $\boldsymbol{U}^0=\boldsymbol{U}^{e,0}$.

Inductive Step: Now we assume that $\boldsymbol{U}^k=\boldsymbol{U}^{e,k}$ holds for some $k\in\mathbb{N}$. From this assumption we want to deduce that $\boldsymbol{U}^{k+1}=\boldsymbol{U}^{e,k+1}$.

Considering the well-balanced properties of the semi-discrete methods in Lemma 3.1 and Lemma 3.3. By comparing the results with the ALE-DG scheme for $\boldsymbol{U}^e$ in (3.7) (again discretized in time via the same modified TVD-RK methods), we have

$$\int_{K^{k+1}}(\boldsymbol{U}^{k+1}-\boldsymbol{U}^{e,k+1})\cdot\boldsymbol{\varphi}^{k+1}\mathrm{d}\boldsymbol{x}=0,\tag{3.30}$$

which leads to $\boldsymbol{U}^{k+1}=\boldsymbol{U}^{e,k+1}$. This finishes the proof of the well-balanced property for the fully discrete methods. □

4. The positivity-preserving well-balanced ALE-DG methods

In this section, we show that the cell average of the numerical solution of the fully-discrete ALE-DG schemes satisfies the weak positivity property under a suitable choice of time step. The limiter introduced in [52] is then applied to enforce the positivity-preserving property of the proposed methods.

4.1. Quadrature rules

We start with introducing the following two sets of quadrature rules to be used in the proofs.

Gauss quadrature rule: In the numerical implementation, the standard Gauss quadrature rule is used for all the integrals appearing in both one-dimensional and two-dimensional fully discrete ALE-DG methods. We denote the two-dimensional Gauss quadrature nodes and weights on the cell $K(t)$ by $\left\{\hat{\boldsymbol{x}}^{\mu}_{K(t)}, \hat{\omega}^{\mu}_{K(t)}\right\}_{1\le\mu\le L}$, which implies that the average of the polynomial $\boldsymbol{U}_{K(t)}$ can be written as

$$\bar{\boldsymbol{U}}_{K(t)} = \sum_{\mu=1}^{L} \hat{\omega}^{\mu}_{K(t)} \boldsymbol{U}_{K(t)}\left(\hat{\boldsymbol{x}}^{\mu}_{K(t)}\right). \tag{4.1}$$

We also denote the one-dimensional Gauss quadrature nodes and weights on the cell edge $F^{\nu}_{K(t)}$ of the cell $K(t)$ by $\left\{\tilde{\boldsymbol{x}}^{\mu}_{F^{\nu}_{K(t)}}, \tilde{\varpi}^{\mu}_{F^{\nu}_{K(t)}}\right\}_{1\le\mu\le N}$, which implies that

$$\int_{F^{\nu}_{K(t)}} \boldsymbol{G}(\boldsymbol{\omega},\boldsymbol{U})\, ds \approx \left|F^{\nu}_{K(t)}\right| \sum_{\mu=1}^{N} \tilde{\varpi}^{\mu}_{F^{\nu}_{K(t)}} \boldsymbol{G}\left(\boldsymbol{\omega}\left(\tilde{\boldsymbol{x}}^{\mu}_{F^{\nu}_{K(t)}}\right), \boldsymbol{U}\left(\tilde{\boldsymbol{x}}^{\mu}_{F^{\nu}_{K(t)}}\right)\right), \tag{4.2}$$

where $\left|F^{\nu}_{K(t)}\right|$ denotes the area of the cell face $F^{\nu}_{K(t)}$. We note that all these quadrature rules should be exact for integrals of polynomials of degrees up to k, since integration by parts on the polynomial integration will be used in the proof of well-balanced property, and this only holds with exact integration of these polynomials.

Special quadrature rule: The special quadrature rule is introduced in [52, Fig. 3.2] to deal with the unstructured mesh. Such a quadrature rule is introduced in this paper only for the purpose of proving the weak positivity property and will not be used in the implementation. The most important property of the special quadrature rule is that

- The quadrature rule has positive weights and is exact for integrals of polynomials of degree up to k on the cell $K(t)$;
- The set of the quadrature points must include all the quadrature points $\tilde{\boldsymbol{x}}^{\mu}_{F^{\nu}_{K(t)}}, \mu = 1,\cdots,N$ on the edges $F^{\nu}_{K(t)} \in \partial K, \nu = 1,\cdots,d+1$.

We can write the average of $\boldsymbol{U}$ over the element $K(t)$ as

$$\bar{\boldsymbol{U}}_{K(t)} = \sum_{\nu=1}^{d+1}\sum_{\mu=1}^{N} \tilde{\omega}^{\mu}_{F^{\nu}_{K(t)}} \boldsymbol{U}^{int_{K(t)}}\left(\tilde{\boldsymbol{x}}^{\mu}_{F^{\nu}_{K(t)}}\right) + \sum_{\mu=1}^{\tilde{L}} \tilde{\omega}^{\mu}_{K(t)} \boldsymbol{U}_{K(t)}\left(\tilde{\boldsymbol{x}}^{\mu}_{K(t)}\right), \tag{4.3}$$

where $\left\{\tilde{\boldsymbol{x}}^{\mu}_{F^{\nu}_{K(t)}}\right\}$ are quadrature points on the boundary of $K(t)$ and $\left\{\tilde{\boldsymbol{x}}^{\mu}_{K(t)}\right\}$ are quadrature points inside K, and $\left\{\tilde{\omega}^{\mu}_{F^{\nu}_{K(t)}}\right\}$ and $\left\{\tilde{\omega}^{\mu}_{K(t)}\right\}$ are the corresponding quadrature weights.

For simplicity, we define the following quadrature nodes set in the cell $K(t)$

$$\begin{aligned}\mathbb{S}_{K(t)} = &\left\{\tilde{\boldsymbol{x}}^{\mu}_{F^{\nu}_{K(t)}}, \mu = 1,\cdots,N, \nu = 1,\cdots,d+1\right\} \bigcup \left\{\tilde{\boldsymbol{x}}^{\mu}_{K(t)}, \mu = 1,\cdots,\tilde{L}\right\} \\ &\bigcup \left\{\hat{\boldsymbol{x}}^{\mu}_{K(t)}, \mu = 1,\cdots,L\right\},\end{aligned} \tag{4.4}$$

and quadrature nodes set on the boundary of $K(t)$

$$\mathbb{Q}_{K(t)} = \left\{\tilde{\boldsymbol{x}}^{\mu}_{F^{\nu}_{K(t)}}, \mu = 1,\cdots,N, \nu = 1,\cdots,d+1\right\}. \tag{4.5}$$

4.2. Properties of the admissible states

The density ρ and the pressure p should stay positive. Numerically, the appearance of negative density or pressure may lead to the breakdown of the simulation, and we hope the numerical solution $\boldsymbol{U}$ can belong to the following set of physically admissible states

$$\mathcal{G} := \left\{\boldsymbol{U} = (\rho, \boldsymbol{m}, E)^T \,\middle|\, \rho > 0,\ \mathcal{E}(\boldsymbol{U}) := E - \frac{\|\boldsymbol{m}\|^2}{2\rho} > 0\right\}, \tag{4.6}$$

where $\mathcal{E}(\boldsymbol{U}) > 0$ is equivalent to the pressure $p > 0$. To prove the weak positivity property satisfied by the cell average of the proposed well-balanced ALE methods, we will introduce some properties of the admissible set $\mathcal{G}$. One can easily verify that the admissible state set $\mathcal{G}$ is convex.

Lemma 4.1 *([38, Lemma 2.3]). For any $\lambda_1 > 0$, $\lambda_0 \ge 0$, $\boldsymbol{U}^1$, $\boldsymbol{U}^0 \in \mathcal{G}$, we have*

$$\lambda_1 \boldsymbol{U}^1 + \lambda_0 \boldsymbol{U}^0 \in \mathcal{G}. \tag{4.7}$$

The following lemma, similar to those lemmas in [51], is introduced for the numerical flux. The main difference to those in [51] is that the numerical flux of the ALE-DG methods involves the grid velocity $\boldsymbol{\omega}$.

Lemma 4.2. *For $\boldsymbol{U} \in \mathcal{G}$, we have*

$$\boldsymbol{U} - \eta \boldsymbol{G}(\boldsymbol{\omega},\boldsymbol{U})\cdot\boldsymbol{n} \in \mathcal{G} \tag{4.8}$$

if $\eta > 0$ and satisfies

$$\alpha_0 \eta \le 1, \tag{4.9}$$

where

$$\alpha_0 := |(\boldsymbol{u}-\boldsymbol{\omega})\cdot\boldsymbol{n}| + \frac{p}{\rho\sqrt{2e}}, \quad \|\boldsymbol{n}\| = 1.$$

Proof. It is easy to check the first component of the vector is positive, following the same proof in [51]. Next, we verify that the pressure of the vector is positive. Simple algebra leads to

$$\begin{aligned}
&\mathcal{E}(\boldsymbol{U} - \eta \boldsymbol{G}(\boldsymbol{\omega},\boldsymbol{U})\cdot\boldsymbol{n}) \\
&= E - \eta\left(E(\boldsymbol{u}-\boldsymbol{\omega})\cdot\boldsymbol{n} + p\boldsymbol{u}\cdot\boldsymbol{n}\right) - \frac{1}{2}\frac{\|\boldsymbol{m} - \eta(((\boldsymbol{u}-\boldsymbol{\omega})\cdot\boldsymbol{n})\boldsymbol{m} + p\boldsymbol{n})\|^2}{\rho - \eta\rho(\boldsymbol{u}-\boldsymbol{\omega})\cdot\boldsymbol{n}} \\
&= (1-\eta(\boldsymbol{u}-\boldsymbol{\omega})\cdot\boldsymbol{n})E - \eta p\boldsymbol{u}\cdot\boldsymbol{n} - \frac{1}{2}\frac{\|(1-\eta(\boldsymbol{u}-\boldsymbol{\omega})\cdot\boldsymbol{n})\boldsymbol{m} - \eta p\boldsymbol{n}\|^2}{(1-\eta(\boldsymbol{u}-\boldsymbol{\omega})\cdot\boldsymbol{n})\rho} \\
&= (1-\eta(\boldsymbol{u}-\boldsymbol{\omega})\cdot\boldsymbol{n})E - \eta p\boldsymbol{u}\cdot\boldsymbol{n} \\
&\quad - \frac{1}{2}\frac{\|(1-\eta(\boldsymbol{u}-\boldsymbol{\omega})\cdot\boldsymbol{n})\rho\boldsymbol{u}\|^2 + (\eta p)^2 - 2\eta(1-\eta(\boldsymbol{u}-\boldsymbol{\omega})\cdot\boldsymbol{n})\rho p\boldsymbol{u}\cdot\boldsymbol{n}}{(1-\eta(\boldsymbol{u}-\boldsymbol{\omega})\cdot\boldsymbol{n})\rho} \\
&= (1-\eta(\boldsymbol{u}-\boldsymbol{\omega})\cdot\boldsymbol{n})\left(E - \frac{1}{2}\rho\|\boldsymbol{u}\|^2\right) - \frac{\eta^2 p^2}{2(1-\eta(\boldsymbol{u}-\boldsymbol{\omega})\cdot\boldsymbol{n})\rho} \\
&= (1-\eta(\boldsymbol{u}-\boldsymbol{\omega})\cdot\boldsymbol{n})\rho e - \frac{\eta^2 p^2}{2(1-\eta(\boldsymbol{u}-\boldsymbol{\omega})\cdot\boldsymbol{n})\rho} \\
&= \frac{\eta^2}{2(1-\eta(\boldsymbol{u}-\boldsymbol{\omega})\cdot\boldsymbol{n})\rho}\left(2\left(\frac{1}{\eta} - (\boldsymbol{u}-\boldsymbol{\omega})\cdot\boldsymbol{n}\right)^2\rho^2 e - p^2\right).
\end{aligned}$$

Now it is easy to verify that, under the condition (4.9), we have

$$1 - \eta(\boldsymbol{u}-\boldsymbol{\omega})\cdot\boldsymbol{n} \ge 1 - \frac{(\boldsymbol{u}-\boldsymbol{\omega})\cdot\boldsymbol{n}}{\alpha_0} > 0, \tag{4.10}$$

and

$$2\left(\frac{1}{\eta} - (\boldsymbol{u}-\boldsymbol{\omega})\cdot\boldsymbol{n}\right)^2\rho^2 e - p^2 \ge 2\left(\alpha_0 - (\boldsymbol{u}-\boldsymbol{\omega})\cdot\boldsymbol{n}\right)^2\rho^2 e - p^2 = 0. \tag{4.11}$$

Therefore, we can conclude that $\boldsymbol{U} - \eta\boldsymbol{G}(\boldsymbol{\omega},\boldsymbol{U})\cdot\boldsymbol{n} \in \mathcal{G}$. □

The following two lemmas are introduced for the HLLC numerical flux. Our proofs are similar to that of [38, Lemmas 2.7, 2.8] and the main difference is that unstructured meshed are considered here and the numerical flux involves the grid velocity.

Lemma 4.3. *For $\boldsymbol{U}^{int}$, $\boldsymbol{U}^{ext} \in \mathcal{G}$, the intermediate states defined in (2.19) and (2.20) satisfy*

$$\boldsymbol{U}^{int,*} \in \mathcal{G}, \quad \boldsymbol{U}^{ext,*} \in \mathcal{G}. \tag{4.12}$$

The proof is the same as the one on static mesh in [4] by replacing $\boldsymbol{u}\cdot\boldsymbol{n}$ with $(\boldsymbol{u}-\boldsymbol{\omega})\cdot\boldsymbol{n}$. Also, the result in [31] shows the same claim for the ALE schemes. Therefore we omit the proof of this lemma in this paper.

Lemma 4.4. *For $\boldsymbol{U}^1$, $\boldsymbol{U}^2 \in \mathcal{G}$ and $\|\boldsymbol{n}\| = 1$, we have*

$$\boldsymbol{U}^1 - \eta\,\hat{\boldsymbol{G}}\left(\boldsymbol{\omega}, \boldsymbol{U}^1, \boldsymbol{U}^2, \boldsymbol{n}\right) \in \mathcal{G}, \tag{4.13}$$

if $\eta > 0$ and satisfies

$$\alpha_0\,\eta \le \frac{1}{2}, \tag{4.14}$$

where

$$\alpha_0 := \max_{\boldsymbol{U}\in\{\boldsymbol{U}^1,\boldsymbol{U}^2\}} |(\boldsymbol{u}-\boldsymbol{\omega})\cdot\boldsymbol{n}| + \sqrt{\gamma p/\rho}.$$

Proof. The proof on static meshes with $\boldsymbol{\omega} = 0$ can be found in [38, Lemma 2.8], and similar proof is also shown in [10] with the Lagrangian scheme. Let $S = S^{int}(\boldsymbol{U}^1, \boldsymbol{U}^2)$, as defined in (2.25), and it satisfies that $2\eta\,|S| < 1$ following the assumption. According to the definition of the HLLC flux, we derive that

$$\begin{aligned}
&\frac{1}{2}\,\boldsymbol{U}^1 - \eta\left(\hat{\boldsymbol{G}}\left(\boldsymbol{\omega}, \boldsymbol{U}^1, \boldsymbol{U}^2, \boldsymbol{n}\right) - \boldsymbol{G}\left(\boldsymbol{\omega}, \boldsymbol{U}^1\right)\cdot\boldsymbol{n}\right)\\
&= \frac{1}{2}\left((2\eta\min(S,0)+1)\boldsymbol{U}^1 + \int_{2\eta\min(S,0)}^{0} \mathcal{R}(x/t, \boldsymbol{U}^1, \boldsymbol{U}^2)\mathrm{d}\boldsymbol{x}\right),
\end{aligned}$$

where $\mathcal{R}(x/t, \boldsymbol{U}^1, \boldsymbol{U}^2)$ denotes the approximate HLLC solution to the Riemann problem between the state $\boldsymbol{U}^1$ and $\boldsymbol{U}^2$, i.e.,

$$\mathcal{R}(x/t, \boldsymbol{U}^1, \boldsymbol{U}^2) = \begin{cases} \boldsymbol{U}^1, & \text{if } \frac{x}{t} \le S^{int}, \\ \boldsymbol{U}^{1,*}, & \text{if } S^{int} \le \frac{x}{t} \le S^{M}, \\ \boldsymbol{U}^{2,*}, & \text{if } S^{M} \le \frac{x}{t} \le S^{ext}, \\ \boldsymbol{U}^{2}, & \text{if } \frac{x}{t} \ge S^{ext}. \end{cases} \tag{4.15}$$

We have $\mathcal{R}(x/t, \boldsymbol{U}^1, \boldsymbol{U}^2) \in \mathcal{G}$ due to Lemma 4.3, and the convexity of $\mathcal{G}$ leads to

$$\frac{1}{2}\boldsymbol{U}^1 - \eta\left(\hat{\boldsymbol{G}}\left(\boldsymbol{\omega}, \boldsymbol{U}^1, \boldsymbol{U}^2, \boldsymbol{n}\right) - \boldsymbol{G}\left(\boldsymbol{\omega}, \boldsymbol{U}^1\right)\cdot\boldsymbol{n}\right) \in \mathcal{G}. \tag{4.16}$$

Moreover, using Lemma 4.2 and the condition (4.14), we have

$$\frac{1}{2}\boldsymbol{U}^1 - \eta\,\boldsymbol{G}\left(\boldsymbol{\omega}, \boldsymbol{U}^1\right)\cdot\boldsymbol{n} \in \mathcal{G}. \tag{4.17}$$

Combining the results in (4.16) and (4.17), we have

$$\boldsymbol{U}^1 - \eta\,\hat{\boldsymbol{G}}\left(\boldsymbol{\omega}, \boldsymbol{U}^1, \boldsymbol{U}^2, \boldsymbol{n}\right) \in \mathcal{G},$$

following the convexity of $\mathcal{G}$. □

The following two lemmas are introduced to address the impact of the well-balanced modifications of the numerical flux terms and source term approximation, respectively.

Lemma 4.5 *([49, Lemma 4.3]). For $\boldsymbol{U}$, $\boldsymbol{U}^* \in \mathcal{G}$ with $\boldsymbol{u} = \boldsymbol{u}^*$, we have*

$$\boldsymbol{U} - \eta\,\boldsymbol{U}^* \in \mathcal{G} \tag{4.18}$$

if $\eta > 0$ and satisfies

$$\alpha_1\,\eta \le 1 \tag{4.19}$$

where

$$\alpha_1 = \max\left(\frac{\rho^*}{\rho}, \frac{p^*}{p}\right).$$

Lemma 4.6 *([38, Lemma 2.4]). For $\lambda > 0$, $\eta \in \mathbb{R}$, $\boldsymbol{U} \in \mathcal{G}$, and $\boldsymbol{a} \in \mathbb{R}^d$, if $|\eta|\frac{\|\boldsymbol{a}\|}{\sqrt{2e}} \le \lambda$, then*

$$\lambda\boldsymbol{U} - \eta(0, \rho\boldsymbol{a}, \boldsymbol{m}\cdot\boldsymbol{a})^T \in \mathcal{G}. \tag{4.20}$$

4.3. The positivity-preserving property

In this section, we will prove that both of the proposed well-balanced schemes satisfy a weak positivity property. A simple scaling limiter can be applied to enforce the positivity-preserving property.

4.3.1. The weak positivity property

We list the weak positivity property of two proposed schemes below and refer to Appendix A and B for the detailed proofs, respectively.

Theorem 4.7 *(Hydrostatic reconstruction). For the semi-discrete scheme (3.14) and time discretization (3.28), if $\boldsymbol{U}_K^n(x) \in \mathcal{G}$ holds for any $x \in \mathbb{S}_K^n$, we have*

$$\bar{\boldsymbol{U}}_K^{n+1} \in \mathcal{G} \tag{4.21}$$

under the CFL-type condition

$$\hat{\alpha}_0\Delta t \le 1 \tag{4.22}$$

with

$$\hat{\alpha}_0 = \hat{\alpha}_F + \hat{\alpha}_S,$$

$$\hat{\alpha}_F = \hat{\alpha}_1\,\alpha \max_{v,\mu} \frac{2\tilde{\varpi}^{\mu}_{F_{K^n}^{v}}|F_{K^n}^{v}|}{\tilde{\omega}^{\mu}_{F_{K^n}^{v}}\Delta_{K^n}}, \qquad \alpha = \max_{\boldsymbol{x}\in\mathbb{Q}_{K^n}} |(\boldsymbol{u}_K^b(\boldsymbol{x}) - \boldsymbol{\omega})\cdot\boldsymbol{n}| + \sqrt{\gamma\frac{p_K^b(\boldsymbol{x})}{\rho_K^b(\boldsymbol{x})}},$$

$$\hat{\alpha}_1 = \max_{\boldsymbol{x}\in\mathbb{Q}_{K^n}} \left(\frac{\rho_K^b(\boldsymbol{x})}{\rho_K^n(\boldsymbol{x})}, \frac{p_K^b(\boldsymbol{x})}{p_K^n(\boldsymbol{x})}\right), \qquad \hat{\alpha}_S = \max_{\boldsymbol{x}\in\mathbb{S}_{K^n}} \frac{\|\nabla p_K^{\tilde{e},n}(\boldsymbol{x})/\rho_K^{e,n}(\boldsymbol{x})\|}{\sqrt{2e_K^n(\boldsymbol{x})}},$$

where $\bar{\boldsymbol{U}}_K^{n+1}$ denotes the average of numerical solution $\boldsymbol{U}_K^{n+1}$.

Theorem 4.8 *(Special source term). For the semi-discrete scheme (3.20) and time discretization (3.28), if $\boldsymbol{U}_K^n(x) \in \mathcal{G}$ holds for any $x \in \mathbb{S}_K^n$, we have*

$$\bar{\boldsymbol{U}}_K^{n+1} \in \mathcal{G} \tag{4.23}$$

under the CFL-type condition

$$\tilde{\alpha}_0\Delta t \le 1 \tag{4.24}$$

with

$$\tilde{\alpha}_0 = \tilde{\alpha}_F + \tilde{\alpha}_S,$$

$$\tilde{\alpha}_F = \alpha\tilde{\alpha}_1 \max_{v,\mu} \frac{2\tilde{\varpi}^{\mu}_{F_K^{v}}|F_{K^n}^{v}|}{\tilde{\omega}^{\mu}_{F_{K^n}^{v}}\Delta_{K^n}}, \qquad \tilde{\alpha}_1 = \max_{\boldsymbol{x}\in\mathbb{Q}_{K^n}} \frac{p^c(\boldsymbol{x})}{p^e(\boldsymbol{x})},$$

$$\alpha = \max_{\boldsymbol{x}\in\mathbb{Q}_{K^n}} |(\boldsymbol{u}_K^{\tilde{b}}(\boldsymbol{x}) - \boldsymbol{\omega})\cdot\boldsymbol{n}| + \sqrt{\gamma\frac{p_K^{\tilde{b}}(\boldsymbol{x})}{\rho_K^{\tilde{b}}(\boldsymbol{x})}}, \qquad \tilde{\alpha}_S = \tilde{\alpha}_S^1 + \tilde{\alpha}_S^2,$$

$$\tilde{\alpha}_S^1 = \max_{\boldsymbol{x}\in\mathbb{S}_{K^n}} \frac{\|\nabla p_K^{e,n}(\boldsymbol{x})/\rho_K^{e,n}(\boldsymbol{x})\|}{\sqrt{2e_K^n(\boldsymbol{x})}}, \qquad \tilde{\alpha}_S^2 = \frac{\|\int_{\partial K^n}[p]^{e,K^n}\boldsymbol{n}\mathrm{d}s\|}{\Delta_{K^n}\bar{\rho}^e\sqrt{2\bar{e}_K^n}},$$

where $[p]^{e,K^n} = (p^{e,ext_{K^n}} - p^{e,int_{K^n}})/2$.

Remark 4.9. We note that the term $T = \max_{v,\mu} \frac{\tilde{\varpi}^{\mu}_{F_{K^n}^{v}}|F_{K^n}^{v}|}{\tilde{\omega}^{\mu}_{F_{K^n}^{v}}\Delta_{K^n}}$ in the parameters $\hat{\alpha}_F$ and $\tilde{\alpha}_F$ is based on the shape of the triangle cells and the quadrature rule. A further discussion on the size of this term can be found in [49, Remark 4.1]. For example, $T = \frac{6}{\Delta_{K^n}}$ in one dimension and

$T \approx \frac{19.3}{\sqrt{\Delta_{K^n}}}$ for a 30-60-90 triangle in two dimensions with the polynomial degree $k = 2$.

4.3.2. The positivity-preserving limiter

Based on the weak positivity properties introduced in Section 4.3.1, a positivity-preserving limiter is presented in [52] on the static mesh. The same limiter approach can be extended to the ALE-DG methods. Under the assumption that $\bar{\boldsymbol{U}}_{K(t)} \in \mathcal{G}$, such limiter can be implemented in two steps.

The first step is to ensure the positivity of density via

$$\hat{\boldsymbol{U}}_{K(t)}(\boldsymbol{x}) = \left(\hat{\rho}_{K(t)}(\boldsymbol{x}), \boldsymbol{m}_{K(t)}(\boldsymbol{x}), E_{K(t)}(\boldsymbol{x})\right)^T, \tag{4.25}$$

$$\hat{\rho}_{K(t)} = \theta^{(1)}_{K(t)}\left(\rho_{K(t)} - \bar{\rho}_{K(t)}\right) + \bar{\rho}_{K(t)}, \tag{4.26}$$

$$\theta^{(1)}_{K(t)} = \min\left\{1, \frac{\bar{\rho}_{K(t)} - \epsilon}{\bar{\rho}_{K(t)} - \min_{\boldsymbol{x}\in\mathbb{S}_{K(t)}} \rho_{K(t)}(\boldsymbol{x})}\right\}. \tag{4.27}$$

The resulting density $\hat{\rho}_{K(t)}(\boldsymbol{x})$ is positive for all $\boldsymbol{x} \in \mathbb{S}_{K(t)}$.

The second step is to ensure the positivity of pressure via

$$\tilde{\boldsymbol{U}}_{K(t)} = \theta^{(2)}_{K(t)}\left(\hat{\boldsymbol{U}}_{K(t)}(\boldsymbol{x}) - \bar{\boldsymbol{U}}_{K(t)}\right) + \bar{\boldsymbol{U}}_{K(t)}, \tag{4.28}$$

$$\theta^{(2)}_{K(t)} = \min\left\{1, \frac{\mathcal{E}\left(\bar{\boldsymbol{U}}_{K(t)}\right) - \epsilon}{\mathcal{E}\left(\bar{\boldsymbol{U}}_{K(t)}\right) - \min_{\boldsymbol{x}\in\mathbb{S}_{K(t)}} \mathcal{E}\left(\hat{\boldsymbol{U}}_{K(t)}(\boldsymbol{x})\right)}\right\}. \tag{4.29}$$

One can show that $\tilde{\boldsymbol{U}}_{K(t)} \in \mathcal{G}$, and then treat it as the updated numerical solution to continue the simulation. We apply the limiter at each Runge-Kutta stage in our simulation and still denote the obtained numerical solution by $\boldsymbol{U}_{K(t)}$ for simplicity. We note that this positivity-preserving limiter is very important to the robustness of the numerical simulations. Without such a limiter, the weak positivity property cannot hold for all time steps, and in some numerical examples listed below, it will break down quickly.

Remark 4.10. We note that this positivity-preserving limiter won't destroy the well-balanced property. In our method, we apply the limiter Θ to $\boldsymbol{U}$ and $\boldsymbol{U}^e$ at each Runge-Kutta stage. For the equilibrium state, which involves low density or low pressure, we still have $\boldsymbol{U} = \boldsymbol{U}^e$ and $\boldsymbol{U}^f = 0$. Moreover, we still have $\boldsymbol{U}^{\tilde{e}}$ being continuous at the cell boundary, because the limiter Θ is not applied to $\boldsymbol{U}^{\tilde{e}}$. In this situation, the proof of Proposition 3.4 holds, and the well-balanced property can be maintained.

5. Numerical examples

This section provides numerical results for the proposed two well-balanced schemes. We denote the scheme based on hydrostatic reconstruction (3.14) by WB(H) and the scheme based on a special source term approximation (3.20) by WB(S). In all numerical tests, moving meshes are given arbitrarily, without any special rules. Unless otherwise stated, the following settings for the moving meshes and polynomial degrees are used. In 1D examples, we use the uniform initial mesh coupled with moving grids:

$$x_{j+\frac{1}{2}}(t) = x_{j+\frac{1}{2}}(0) + \frac{1}{10(x_r - x_l)^2}\sin\left(\frac{2\pi t}{T}\right)\left(x_{j+\frac{1}{2}}(0) - x_r\right) \times \left(x_{j+\frac{1}{2}}(0) - x_l\right), \tag{5.1}$$

where T is the stop time and x_l, x_r are the endpoints of the computational domain. In 2D examples, we use the uniform criss-triangular initial mesh coupled with moving grids:

$$\begin{aligned} x_j(t) &= x_j(0) + 0.03\sin\left(\frac{2\pi x_j(0)}{x_r - x_l}\right)\sin\left(\frac{2\pi y_j(0)}{y_r - y_l}\right)\sin\left(\frac{2\pi t}{T}\right), \\ y_j(t) &= y_j(0) + 0.02\sin\left(\frac{2\pi x_j(0)}{x_r - x_l}\right)\sin\left(\frac{2\pi y_j(0)}{y_r - y_l}\right)\sin\left(\frac{4\pi t}{T}\right), \end{aligned} \tag{5.2}$$

Table 5.1
Example 5.1, L^1 errors and orders of accuracy for the scheme WB(H) and $k = 1, 2, 3$.

$k=1$	ρ		ρu		E	
N	L^1 error	order	L^1 error	order	L^1 error	order
50	1.45E-05	–	2.46E-06	–	1.03E-05	–
100	4.17E-06	1.80	6.11E-07	2.01	2.57E-06	2.00
200	1.10E-06	1.93	1.52E-07	2.00	6.43E-07	2.00
400	2.80E-07	1.97	3.81E-08	2.00	1.61E-07	2.00

$k=2$	ρ		ρu		E	
N	L^1 error	order	L^1 error	order	L^1 error	order
10	6.55E-06	–	1.60E-06	–	5.72E-06	–
20	9.60E-07	2.77	1.98E-07	3.02	7.16E-07	3.00
40	1.14E-07	3.08	2.47E-08	3.01	9.00E-08	2.99
80	1.09E-08	3.38	3.08E-09	3.00	1.13E-08	3.00

$k=3$	ρ		ρu		E	
N	L^1 error	order	L^1 error	order	L^1 error	order
5	2.88E-07	–	6.95E-07	–	7.96E-07	–
10	1.62E-08	4.15	4.37E-08	3.99	6.97E-08	3.51
20	1.89E-09	3.11	2.26E-09	4.27	3.47E-09	4.33
40	1.20E-10	3.97	1.38E-10	4.04	2.41E-10	3.85

where x_r, x_l, y_r, y_l are the vertexes of the rectangle computational domain. These grids are not following the fluid velocity, but move around their initial position with a relatively small amplitude to avoid the grid lines crossing. $\mathbb{P}^2$ piecewise polynomials are used in most numerical examples. In Examples 5.3, 5.4 and 5.5, we show that our ALE-DG methods can reduce numerical dissipation if the grid velocity is chosen to be close to the fluid velocity.

For all the positivity-preserving tests in this section, the time step Δt depends both on the constraints in Theorems 4.7, 4.8 and the stability constraints of Runge-Kutta methods. The time step size at each time step is plotted for the positivity-preserving tests in Examples 5.3 and 5.9, and we can observe the time step size won't become extremely small when the density or pressure is close to 0.

5.1. Numerical examples in one dimension

Example 5.1. Accuracy test in 1D.

To demonstrate that the proposed two schemes are high order schemes, we consider a special steady state introduced in [21], which is given by

$$\rho(x,t) = \exp(-x), \quad u(x,t) = 0, \quad p(x,t) = (1+x)\exp(-x),$$

with gravitational field $\phi(x) = \frac{1}{2}x^2$ on the computational domain $[0,1]$. We apply the exact solutions at the domain boundaries to calculate the numerical flux. For the desired equilibrium state $\boldsymbol{U}^d$ in this example, we set a simple isothermal equilibrium state as

$$\rho^d(x,t) = \exp(-\frac{1}{2}x^2), \quad u^d(x,t) = 0, \quad p^d(x,t) = \exp(-\frac{1}{2}x^2).$$

We set the stop time $T = 0.1$, and the L^1 errors and orders are shown in Table 5.1 for scheme WB(H) and Table 5.2 for scheme WB(S). It can be observed that our schemes obtain the optimal order of accuracy. Note that although the exact solution is a steady state, we can still get an error table without round-off errors since we choose a different $\boldsymbol{U}^d$ from the exact solution.

Example 5.2. Well-balanced test of the polytropic equilibrium in 1D.

This example is used to verify that our schemes maintain the polytropic equilibrium and can capture small perturbations for 1D Euler

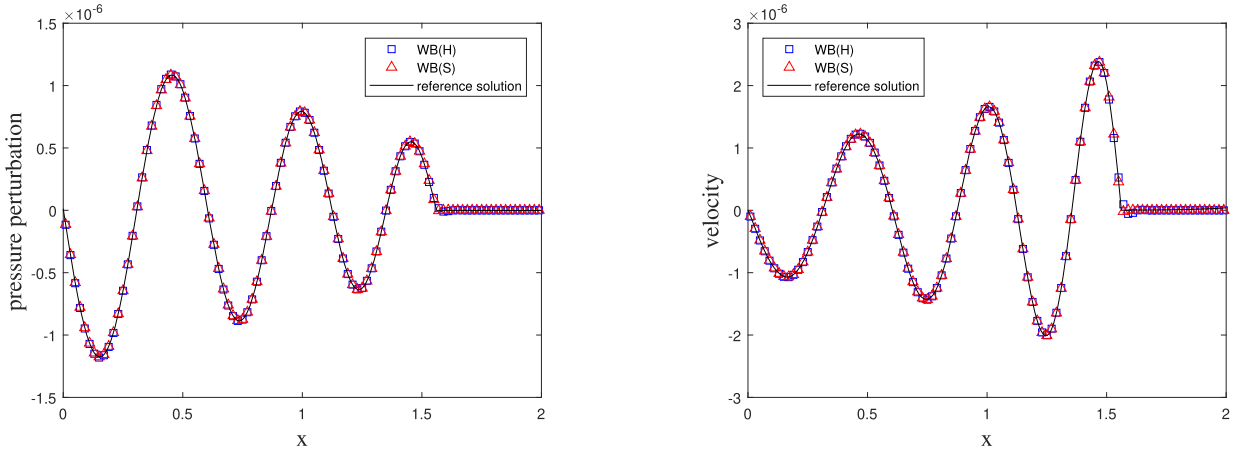

Fig. 5.1. Example 5.2: Small amplitude waves $A = 10^{-6}$ with 100 cells at $T = 1.5$ for scheme WB(H) and WB(S) compared with a reference solution of 2000 cells. Left: pressure perturbation; Right: velocity.

Table 5.2
Example 5.1, L^1 errors and orders of accuracy for the scheme WB(S) and $k = 1, 2, 3$.

$k=1$	ρ		ρu		E	
N	L^1 error	order	L^1 error	order	L^1 error	order
25	1.21E-05	–	4.20E-06	–	1.02E-05	–
50	3.42E-06	1.82	1.05E-06	2.01	2.55E-06	2.00
100	8.95E-07	1.93	2.61E-07	2.00	6.39E-07	2.00
200	2.28E-07	1.97	6.52E-08	2.00	1.60E-07	2.00
$k=2$	ρ		ρu		E	
N	L^1 error	order	L^1 error	order	L^1 error	order
10	5.34E-06	–	1.74E-06	–	6.07E-06	–
20	8.08E-07	2.72	2.19E-07	2.99	7.49E-07	3.02
40	9.36E-08	3.11	2.74E-08	3.00	9.37E-08	3.00
80	9.11E-09	3.36	3.43E-09	3.00	1.18E-08	2.99
$k=3$	ρ		ρu		E	
N	L^1 error	order	L^1 error	order	L^1 error	order
5	3.04E-07	–	6.43E-07	–	8.05E-07	–
10	1.86E-08	4.03	4.01E-08	4.00	7.78E-08	3.37
20	2.17E-09	3.10	2.10E-09	4.26	3.87E-09	4.33
40	1.46E-10	3.89	1.28E-10	4.04	2.76E-10	3.81

equations. We consider the simple set of a polytropic hydrostatic atmosphere under a constant gravitational field in [21]. The desired polytropic equilibrium $\boldsymbol{U}^d$ is given by

$$\rho^d(x) = (\rho_0^{\gamma-1} - \kappa_0 \frac{\gamma-1}{\gamma} g x)^{\frac{1}{\gamma-1}}, \quad u^d(x) = 0, \quad p^d(x) = \kappa_0 (\rho^d(x))^\gamma, \tag{5.3}$$

with gravitational field $\phi(x) = gx$ on a computational domain $[0, 2]$. The constants in this example are given by $g = 1$, $\gamma = \frac{5}{3}$, $\rho_0 = 1$, $\kappa_0 = 1$.

1. **Well-balanced property**
   We set the initial condition as $\boldsymbol{U}^0 = \mathbb{P}^2 \boldsymbol{U}^d$ and the stop time as $T = 2$. We apply the exact solutions at the domain boundaries to calculate the numerical flux. With the mesh size $N = 100$, the L^1 errors for different precision are shown in Table 5.3. It can be observed that both schemes can maintain the polytropic equilibrium state with round-off error, which confirms that our schemes can keep the equilibrium states exactly at a discrete level.
2. **Small perturbation test**
   Next, we impose a periodic velocity perturbation at the bottom of the atmosphere

$$u(0,t) = A \sin(4\pi t),$$

to the polytropic equilibrium $\boldsymbol{U}^d$, i.e. the left boundary condition is given as

$$\rho(0,t) = \rho^d(0), \quad u(0,t) = A\sin(4\pi t), \quad p(0,t) = p^d(0), \tag{5.4}$$

and $\boldsymbol{U}(0,t)$ can be calculated correspondingly. We use the inflow/outflow boundary condition that the left limit of the left boundary is calculated by using (5.4). This example can test the capability of our scheme in capturing the propagation of the small perturbation. We consider the case with a small amplitude $A = 10^{-6}$. The stop time is set as $T = 1.5$ and $N = 100$ cells are employed. The numerical results are shown in Fig. 5.1. We can observe that both schemes can capture the generated wave well.

Example 5.3. Rarefaction test with low density and low pressure.

We consider a rarefaction wave test introduced in [38] to show that our scheme can keep the density and pressure positive. We also generate a special mesh movement to show the advantages of ALE-DG methods. The initial condition is a Riemann problem given by

$$\begin{aligned} &\rho = 7, \quad u = -1, \quad p = 0.2, \quad \text{if } x \le 0, \\ &\rho = 7, \quad u = 1, \quad p = 0.2, \quad \text{if } x \ge 0, \end{aligned} \tag{5.5}$$

with outflow boundary conditions on the computational domain $[-1, 1]$. The gravitation field takes the form $\phi = x^2/2$. We employ $N = 100$ cells and the final stop time as $T = 0.6$. In this example, the initial mesh is simply 800 uniform cells and the final mesh is set as:

$$x_{j+\frac{1}{2}}(0.6) = \begin{cases} -1 + \frac{j}{40} \times 0.3, & \text{for } 0 \le j \le 40, \\ -0.7 + \frac{j-40}{260} \times 0.5, & \text{for } 41 \le j \le 300, \\ -0.2 + \frac{j-300}{200} \times 0.4, & \text{for } 301 \le j \le 500, \\ 0.2 + \frac{j-500}{260} \times 0.5, & \text{for } 501 \le j \le 760, \\ 0.7 + \frac{j-760}{40} \times 0.3, & \text{for } 761 \le j \le 800, \end{cases} \tag{5.6}$$

which leads to the grid velocity set as

$$\omega_{j+\frac{1}{2}}(t) = \frac{x_{j+\frac{1}{2}}(0.6) - x_{j+\frac{1}{2}}(0)}{0.6}, \quad \text{for } t \in [0, 0.6],\ 0 \le j \le 800. \tag{5.7}$$

The same $\boldsymbol{U}^d$ as in Example 5.1 is considered. In Fig. 5.3, we show the results for both schemes compared with a reference solution of 6400 cells and the static mesh solution of 800 cells. From Fig. 5.3, it can be observed that the low pressure and the low density are both maintained positively for the proposed schemes. It also shows that the results of ALE-DG schemes are better than the static mesh results, which is consistent with the impression that ALE-DG methods can reduce nu-

Table 5.3
Example 5.2, L^1 errors of different precision for the polytropic equilibrium $\boldsymbol{U}^d$ using two schemes WB(H) and WB(S).

Precision	WB(H)			WB(S)		
	ρ	ρu	E	ρ	ρu	E
double	7.33E-15	1.89E-15	3.45E-15	6.69E-15	2.03E-15	3.66E-15
quadruple	5.85E-33	1.39E-33	2.64E-33	4.99E-33	1.54E-33	3.00E-33

Table 5.4
Example 5.3, the minimum of density and pressure for two schemes.

Scheme	Density	Pressure
WB(H)	9.30E-03	2.54E-04
WB(S)	8.30E-03	2.38E-04

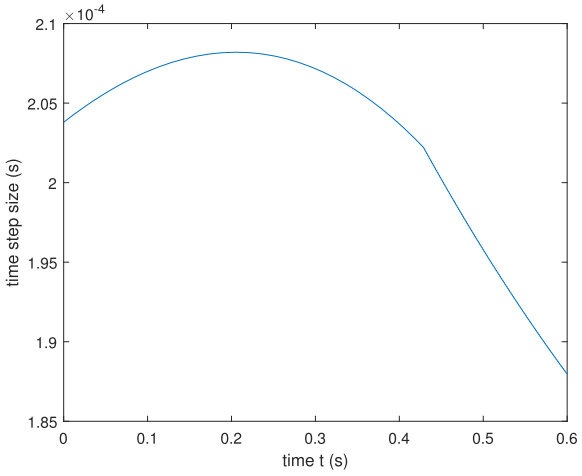

Fig. 5.2. Example 5.3, time step size v.s. time for the scheme WB(S), we can see the time step size is relatively stable during the simulation.

merical dissipation. We also show the minimum density and pressure in Table 5.4 to illustrate that both schemes preserve density and pressure positively. In Fig. 5.2, we plot the time history of the actual time step size, which is calculated according to Theorem 4.8 for the scheme WB(S). It can be observed that the time step size is relatively stable when the density or the pressure is close to 0.

Example 5.4. Shock tube test.

This example is the standard Sod test, coupled with the gravitational field. By following the setup in [42], the computational domain is $[0,1]$, and the initial condition takes the form

$$\begin{aligned} &\rho = 1, && u = 0, \quad p = 1, && \text{if } x \le 0.5, \\ &\rho = 0.125, && u = 0, \quad p = 0.1, && \text{if } x \ge 0.5. \end{aligned} \tag{5.8}$$

The gravitational field is set as $\phi(x) = x$ and $\gamma = 1.4$. The initial mesh contains the 100 uniform cells, and at the final time $T = 0.2$, it becomes the following mesh

$$x_{j+\frac{1}{2}}(0.2) = \begin{cases} \frac{j}{5} \times 0.2, & \text{for } 0 \le j \le 5, \\ 0.2 + \frac{j-5}{30} \times 0.3, & \text{for } 6 \le j \le 35, \\ 0.5 + \frac{j-45}{30} \times 0.25, & \text{for } 36 \le j \le 65, \\ 0.75 + \frac{j-55}{30} \times 0.1, & \text{for } 66 \le j \le 95, \\ 0.85 + \frac{j-95}{5} \times 0.15, & \text{for } 96 \le j \le 100, \end{cases} \tag{5.9}$$

which leads to the grid velocity set as

$$\omega_{j+\frac{1}{2}}(t) = \frac{x_{j+\frac{1}{2}}(0.2) - x_{j+\frac{1}{2}}(0)}{0.2}, \quad \text{for } t \in [0, 0.2],\ 0 \le j \le 100. \tag{5.10}$$

We use the reflective boundary condition. In Fig. 5.4, we show the results for both schemes WB(H) and WB(S) with 100 cells, compared with a reference solution of 2000 cells and a static mesh solution of 100 cells. We can see that both proposed schemes capture the shocks well and have less numerical dissipation for $x \in [0.8, 0.85]$.

Example 5.5. Leblanc problem in a linear gravitational field.

In this example, we consider a Leblanc problem in linear gravitational field $\phi(x) = x$, which is used in [38] to test the positivity-preserving property of schemes. The initial condition of this problem is given by

$$\begin{aligned} &\rho = 2, && u = 0, \quad p = 10^9, && \text{if } x \le 5, \\ &\rho = 0.001, && u = 0, \quad p = 1, && \text{if } x \ge 5. \end{aligned} \tag{5.11}$$

The computational domain is $[0, 10]$ with reflection boundary conditions. For the grid velocity, we set the initial mesh as the 200 uniform cells and the final mesh as

$$x_{j+\frac{1}{2}}(0.25) = \begin{cases} \frac{j}{130} \times 7, & \text{for } 0 \le j \le 130, \\ 7 + \frac{j-130}{60} \times 2, & \text{for } 131 \le j \le 190, \\ 9 + \frac{j-190}{10}, & \text{for } 191 \le j \le 200, \end{cases} \tag{5.12}$$

which leads to the grid velocity set as

$$\omega_{j+\frac{1}{2}}(t) = \frac{x_{j+\frac{1}{2}}(0.00004) - x_{j+\frac{1}{2}}(0)}{0.00004}, \quad \text{for } t \in [0, 0.00004],\ 0 \le j \le 200. \tag{5.13}$$

In Fig. 5.5, we show the results for both schemes at time $T = 0.00004$ on the above moving mesh, compared with the reference solution of $N = 6400$ cells and static mesh solution of $N = 200$ cells. Our schemes maintain the density and pressure positive and capture the discontinuities better than the static mesh solution.

5.2. Numerical examples in two dimensions

Example 5.6. Accuracy test in 2D.

In this example, the high order accuracy of the proposed methods will be tested in two dimensions on moving triangular meshes. We consider the exact solution in [38], which is given by

$$\begin{aligned} &\rho(x, y, t) = 1 + 0.2 \sin(\pi(x + y - 2t)), \\ &\boldsymbol{u}(x, y, t) = 1, \\ &p(x, y, t) = 4.5 + 2t - x - y + 0.2 \cos(\pi(x + y - 2t))/\pi, \end{aligned}$$

with gravitational field $\phi(x, y) = x + y$ and $\gamma = \frac{5}{3}$ on a square domain $[0, 1] \times [0, 1]$. We apply the exact solutions at the boundaries. The desired equilibrium state $\boldsymbol{U}^d$ is set as an isothermal equilibrium state:

$$\rho^d(x, y) = 0.1 \exp(-0.1(x + y)), \quad \boldsymbol{u}^d = 0, \quad p^d(x, y) = \exp(-0.1(x + y)). \tag{5.14}$$

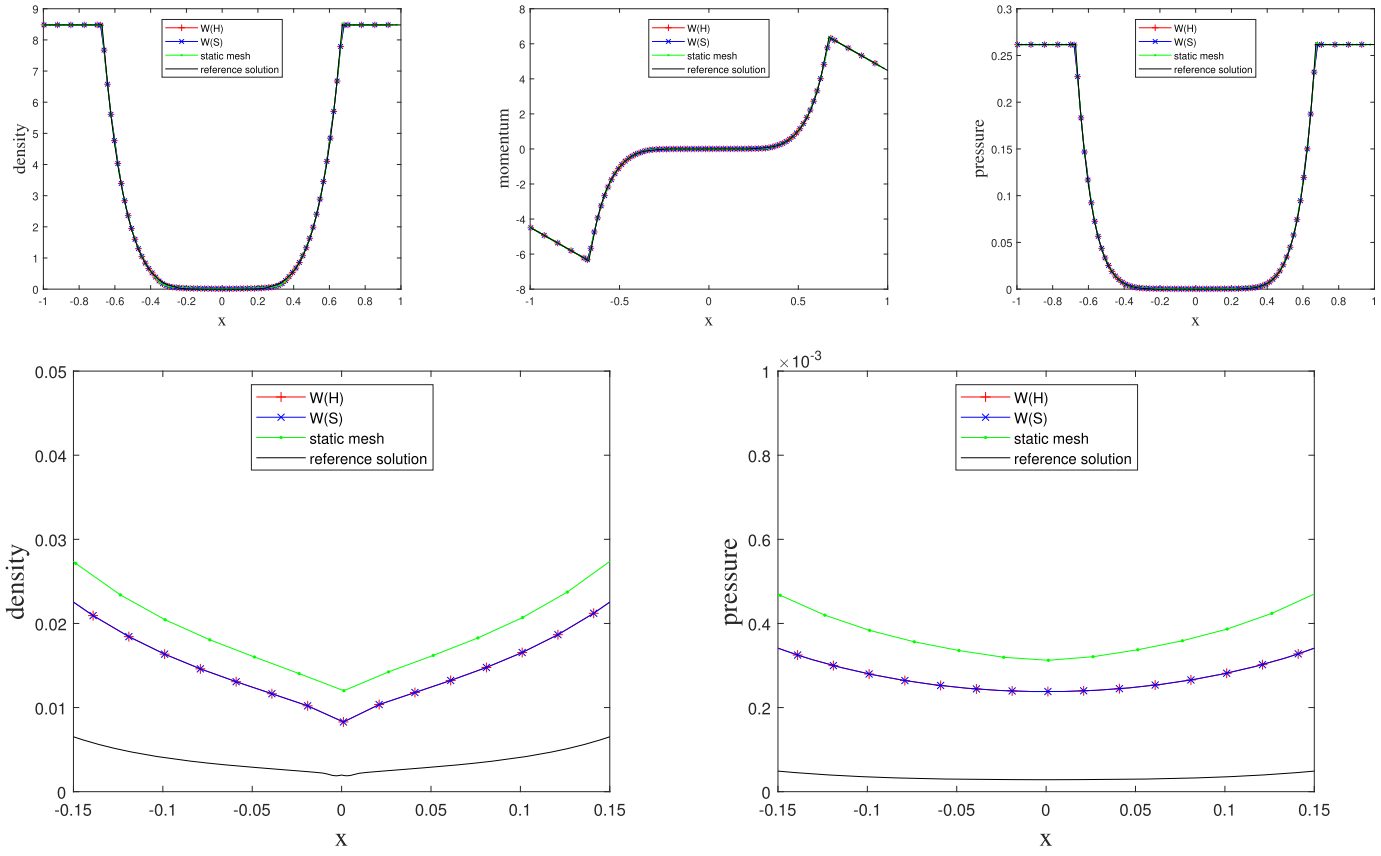

Fig. 5.3. Example 5.3, the top three pictures are density, momentum and pressure at $t = 0.6$ with 800 cells for schemes WB(H) (red), WB(S) (blue), static mesh (green) and reference solution (black). The bottom two pictures are zoom in of density and pressure for $x \in [-0, 15, 0.15]$.

Table 5.5
Example 5.6, L^1 errors and orders of accuracy for the scheme WB(H).

$k = 1$	ρ		ρu		ρv		E	
N	L^1 error	order	L^1 error	order	L^1 error	order	L^1 error	order
200	1.50E-03	–	1.49E-03	–	1.51E-03	–	1.01E-05	–
800	3.76E-04	1.99	3.76E-04	1.99	3.76E-04	2.00	2.52E-06	2.00
3200	9.21E-05	2.03	9.22E-05	2.03	9.21E-05	2.03	6.29E-07	2.00
12800	2.22E-05	2.02	2.27E-05	2.02	2.26E-05	2.02	1.57E-07	2.00
$k = 2$	ρ		ρu		ρv		E	
N	L^1 error	order	L^1 error	order	L^1 error	order	L^1 error	order
200	4.59E-05	–	4.62E-05	–	4.59E-05	–	4.61E-05	–
800	6.08E-06	2.92	6.09E-06	2.93	6.09E-06	2.92	6.07E-06	2.93
3200	7.59E-07	3.00	7.62E-07	3.00	7.63E-07	3.00	7.66E-07	2.99
12800	9.52E-08	2.99	9.61E-08	2.99	9.61E-08	2.99	9.75E-08	2.97

We set the stop time $T = 0.1$ and apply the exact solutions at the domain boundaries to calculate the numerical flux. The L^1 errors and orders for both schemes are shown in Table 5.5 and Table 5.6. We can see that both schemes have the desired high order of accuracy.

Example 5.7. Well-balanced test of the polytropic equilibrium in 2D.

In this example, we consider a simple polytropic equilibrium state in two dimensions:

$$\rho^d(r) = \frac{\sin(\alpha r)}{\alpha r}, \quad \boldsymbol{u}^d(r) = 0, \quad p^d(r) = \rho^d(r)^2,$$

with gravitational field $\phi(r) = -\frac{2\sin(\alpha r)}{\alpha r}$ where $\gamma = 2$, $r = \sqrt{x^2 + y^2}$ and $\alpha = \sqrt{2\pi}$.

We follow the setup in [49] and the computational domain is set as a disc of radius 0.5. The j-th mesh grid at different time levels t is set as follows:

$$x_j(t) = x_j(0) + 0.03\sin(2\pi r_j(0))sin(\frac{2\pi t}{T}),$$

$$y_j(t) = y_j(0) + 0.02\sin(2\pi r_j(0))sin(\frac{4\pi t}{T}).$$

In this example, we test our schemes for maintaining such an equilibrium state and capturing the small perturbation to an equilibrium state.

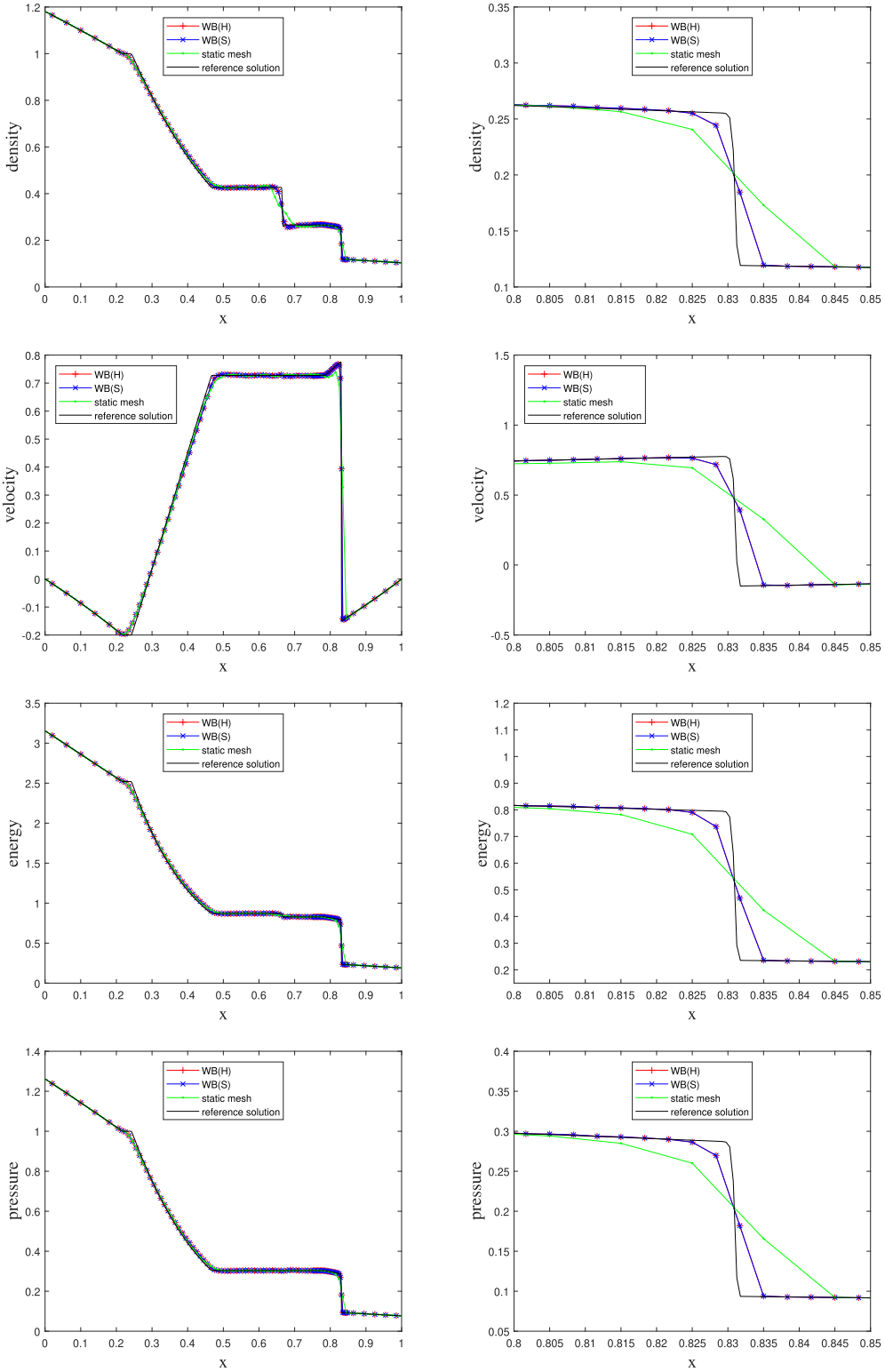

Fig. 5.4. Example 5.4 The numerical results for schemes WB(H) (red) and WB(S) (blue) compared with reference solution (black) and static mesh solution (green). From top to bottom are density, velocity, energy, and pressure. Left are the solutions on the whole computational domain and right are the zoom in for $x \in [0.8, 0.85]$.

1. **Well-balanced property**
   We set the initial condition to be the same as the above polytropic equilibrium state. We use 1222 triangles as the initial mesh. The stop time is set as $T = 1$ and we apply the exact solutions at the domain boundaries to calculate the numerical flux. The L^1 errors for different precision are shown in Table 5.7. We can see our schemes can maintain the polytropic equilibrium.

2. **Small perturbation test**
   Now we consider the case with a small perturbation to the polytropic equilibrium and show the ability to capture the small perturbations of two schemes. The small perturbation is added to the pressure such that

$$\rho(r,0) = \rho^d(r), \quad \boldsymbol{u}(r,0) = 0, \quad p(r,0) = \rho^d(r)^2 + A\exp(-100r^2),$$

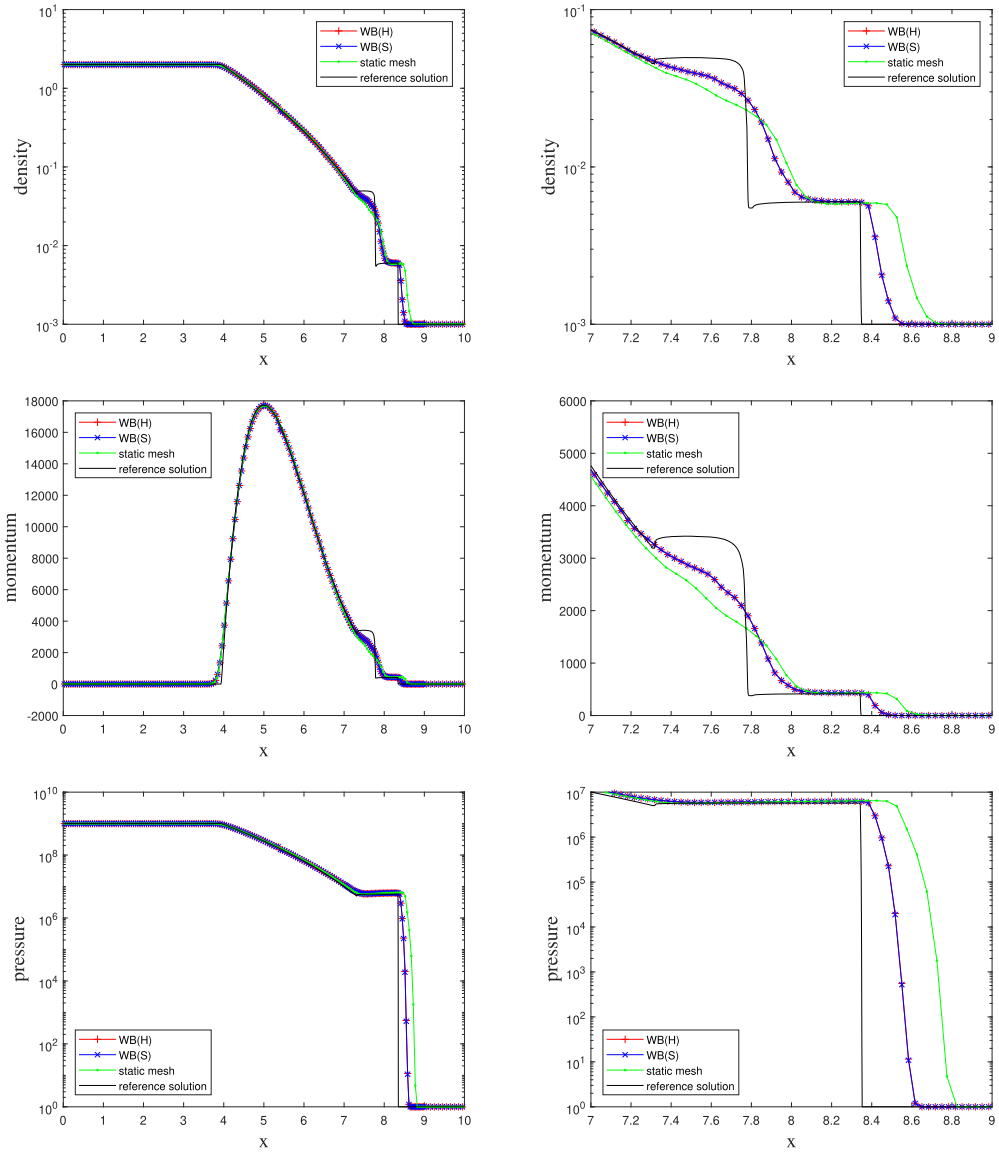

Fig. 5.5. Example 5.5 The numerical results for schemes WB(H) (red) and WB(S) (blue) compared with reference solution (black) and static mesh solution (green). From top to bottom are density, momentum, and pressure. Left are the solutions on the whole computational domain, and right are the zoom-in for $x \in [7,9]$.

Table 5.6
Example 5.6, L^1 errors and orders of accuracy for the scheme WB(S).

$k=1$	ρ		ρu		ρv		E	
N	L^1 error	order	L^1 error	order	L^1 error	order	L^1 error	order
200	1.44E-03	–	1.46E-03	–	1.46E-03	–	1.01E-05	–
800	3.61E-04	2.00	3.64E-04	2.00	3.64E-04	2.00	2.51E-06	2.00
3200	9.00E-05	2.00	9.08E-05	2.00	9.08E-05	2.00	6.29E-07	2.00
12800	2.25E-05	2.00	2.27E-05	2.00	2.27E-05	2.00	1.57E-07	2.00
$k=2$	ρ		ρu		ρv		E	
N	L^1 error	order	L^1 error	order	L^1 error	order	L^1 error	order
200	4.64E-05	–	4.65E-05	–	4.65E-05	–	4.65E-05	–
800	6.06E-06	2.94	6.08E-06	2.94	6.08E-06	2.94	6.08E-06	2.94
3200	7.67E-07	2.98	7.70E-07	2.98	7.70E-07	2.98	7.76E-07	2.97
12800	9.59E-08	3.00	9.66E-08	3.00	9.66E-08	3.00	9.82E-08	2.98

with $A = 10^{-6}$. The stop time is set as $T = 0.2$. The initial mesh is set as a triangular mesh with 4826 triangles. The outflow boundary condition is applied. The numerical results of both proposed methods are provided in Fig. 5.6, from which we observe that both schemes capture the small perturbation correctly.

Example 5.8. Well-balanced test of the isothermal equilibrium in 2D.

In this example, we consider the isothermal equilibrium state in two dimensions:

$$\rho^d(x,y) = \rho_0 \exp(-\frac{\rho_0 g}{p_0}(x+y)), \quad \boldsymbol{u}^d = 0, \quad p^d(x,y) = p_0 \exp(-\frac{\rho_0 g}{p_0}(x+y)),$$

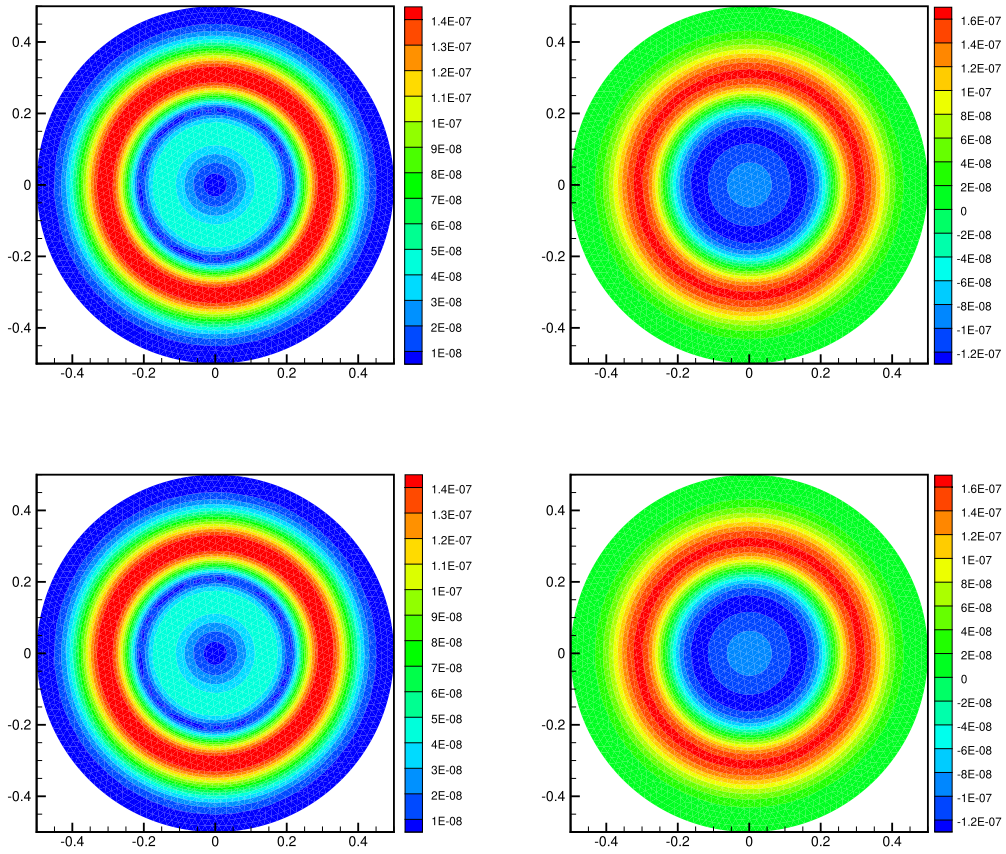

Fig. 5.6. Example 5.7, contours of numerical results of WB(H) scheme and WB(S) scheme with 4826 triangles at $t = 0.2$. Top: WB(H) scheme; Bottom: WB(S) scheme. Left: velocity ($\sqrt{u^2+v^2}$); Right: pressure perturbation.

Table 5.7
Example 5.7, L^1 errors for different precision with 1222 triangles mesh for the polytropic equilibrium.

Scheme	Precision	L^1 error			
		ρ	ρu	ρv	E
WB(H)	double	1.68E-13	4.02E-14	3.50E-14	4.60E-12
	quadruple	1.32E-31	3.44E-32	3.25E-32	3.63E-30
WB(S)	double	2.96E-14	2.81E-15	2.77E-15	3.93E-15
	quadruple	2.52E-32	1.97E-33	1.92E-33	6.58E-33

Table 5.8
Example 5.8, L^1 errors for different precision with 3200 triangles mesh for the isothermal equilibrium.

Scheme	Precision	L^1 error			
		ρ	ρu	ρv	E
WB(H)	double	2.85E-15	6.70E-16	6.31E-16	2.57E-15
	quadruple	1.85E-33	4.60E-34	4.20E-34	1.82E-33
WB(S)	double	3.59E-15	1.21E-15	1.12E-15	4.06E-15
	quadruple	2.47E-33	5.87E-34	5.38E-34	2.17E-33

with the gravitational field $\phi(x,y) = x + y$ and constants $\rho_0 = 1.21$, $p_0 = 1$, $\gamma = 1.4$. The computational domain is set as $[0,1]^2$.

1. **Well-balanced property**
   We set the initial condition to be the same as the desired equilibrium $\boldsymbol{U}^d$. The initial mesh contains the uniform 3200 triangles, and the stop time is set as $T = 0.1$. We apply the exact solutions at the domain boundaries to calculate the numerical flux. The L^1 errors for different precisions are shown in Table 5.8. We can observe that all the errors are at the level of round-off error.
2. **Small perturbation test**
   Next, we add a small perturbation to $\boldsymbol{U}^d$ to the initial equilibrium state $\boldsymbol{U}^d$, and test the capability of our schemes in capturing the propagation of the small perturbation. A small perturbation is added to the pressure such that

$$\rho(x,y,0) = \rho^d(x,y),$$
$$\boldsymbol{u}(x,y,0) = 0,$$
$$p(x,y,0) = \frac{p_0}{\rho_0}\rho^d(x,y) + \epsilon\exp(-121((x-0.3)^2+(y-0.3)^2)),$$

with $\epsilon = 10^{-3}$. The stop time is set as $T = 0.15$ and the initial mesh is set as a uniform 12800 triangles mesh. The outflow boundary condition is applied. Fig. 5.7 shows that our numerical solutions of two schemes capture the perturbation correctly.

Example 5.9. Rarefaction test with low density and low pressure in 2D.

In this example, we want to demonstrate that the proposed schemes can correctly deal with cases involving low density and low pressure. We consider the rarefaction test in [36] with the initial condition given by

$$\rho(x,y) = \exp(-2.5\phi(x,y)), \quad p(x,y) = 0.4\exp(-2.5\phi(x,y)),$$
$$\boldsymbol{u}(x,y) = \begin{cases} (-2,0)^T, & x < 0.5, \\ (2,0)^T, & x > 0.5, \end{cases}$$

with the gravitational field $\phi(x,y) = \frac{1}{2}((x-0.5)^2 + (y-0.5)^2)$ and transmissive boundary conditions. We set the computational domain $[0,1]^2$ with uniform 12800 triangles initial mesh and the stop time as $T = 0.1$. Fig. 5.9 shows the numerical solutions of density, pressure, and mo-

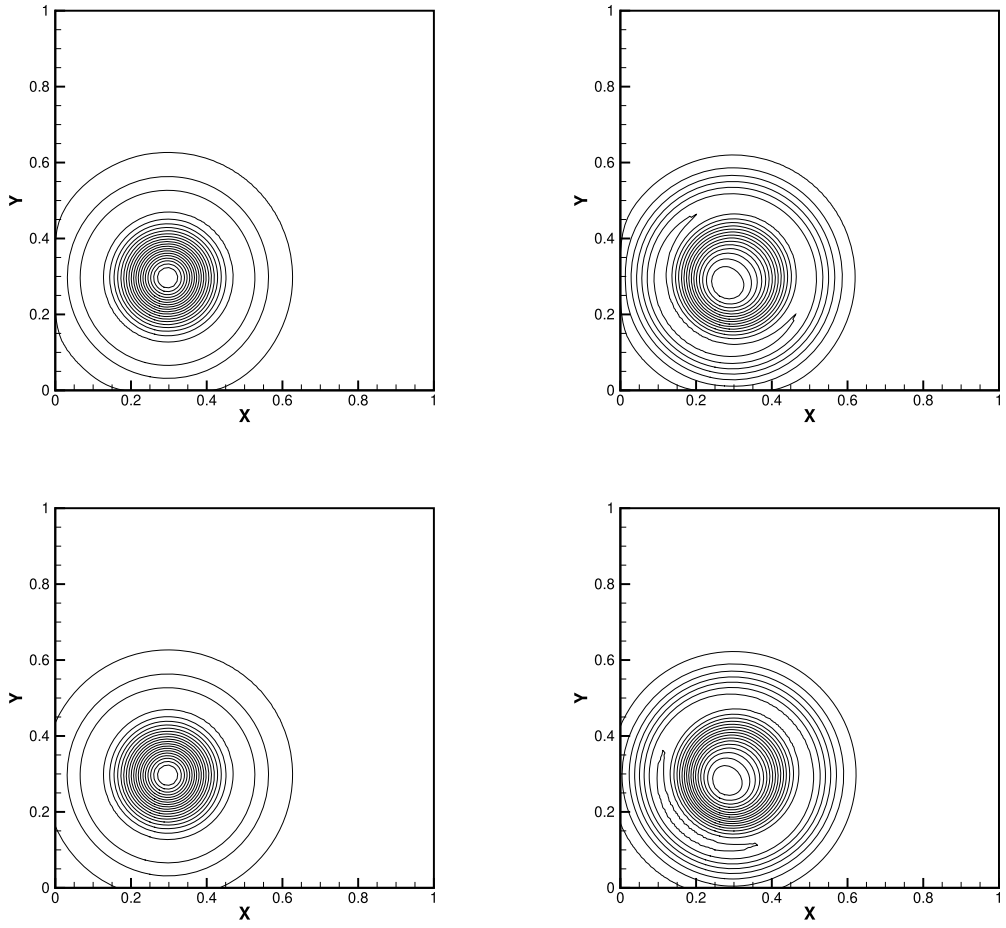

Fig. 5.7. Example 5.8, perturbation on the isothermal hydrostatic solution with $\epsilon = 0.001$ at time $t = 0.15$ with 12800 triangles. Left: the density perturbation with 20 uniformly spaced contour lines from −0.001 to 0.0002; Right: the pressure perturbation with 20 uniformly spaced contour lines from −0.0003 to 0.0003. Top: the results of the scheme WB(H); Bottom: the results of the scheme WB(S).

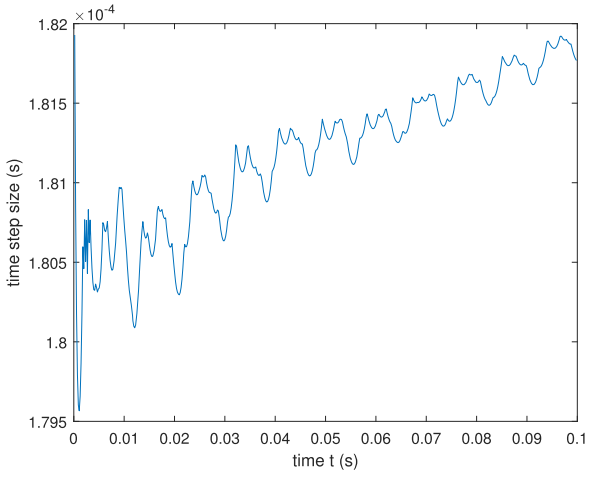

Fig. 5.8. Example 5.9, time step size v.s. time for the scheme WB(S), we can see the time step size is relatively stable during the simulation.

mentum in x-direction m_1. We can see that the proposed schemes keep the low density and low pressure positive in Table 5.9, which lists the minimum density and pressure of both schemes. In Fig. 5.8, we plot the time history of the actual time step size, which is calculated according to Theorem 4.8 for the scheme WB(S). It shows that the time step size doesn't become extremely small when the density or the pressure is close to 0.

Table 5.9
Example 5.9, the minimum density and pressure for two schemes.

scheme	density	pressure
WB(H)	1.26E-02	3.68E-03
WB(S)	6.41E-03	3.03E-03

6. Conclusion

In this paper, we developed the well-balanced ALE-DG methods for moving meshes for the Euler equations with gravitation. By giving the desired equilibrium states, we proposed two different well-balanced methods based on the hydrostatic reconstruction and a special source term approximation, respectively. Both schemes are based on the techniques of DG methods on static meshes, and the extension to moving meshes is carefully investigated in this paper. The resulting methods have a weak positivity property and a simple limiter can be applied to enforce the positivity-preserving property. One- and two-dimensional numerical examples have been provided to show the well-balanced property, high-order accuracy, the advantage of ALE-DG methods, and positivity-preserving property.

Data availability

Data will be made available on request.

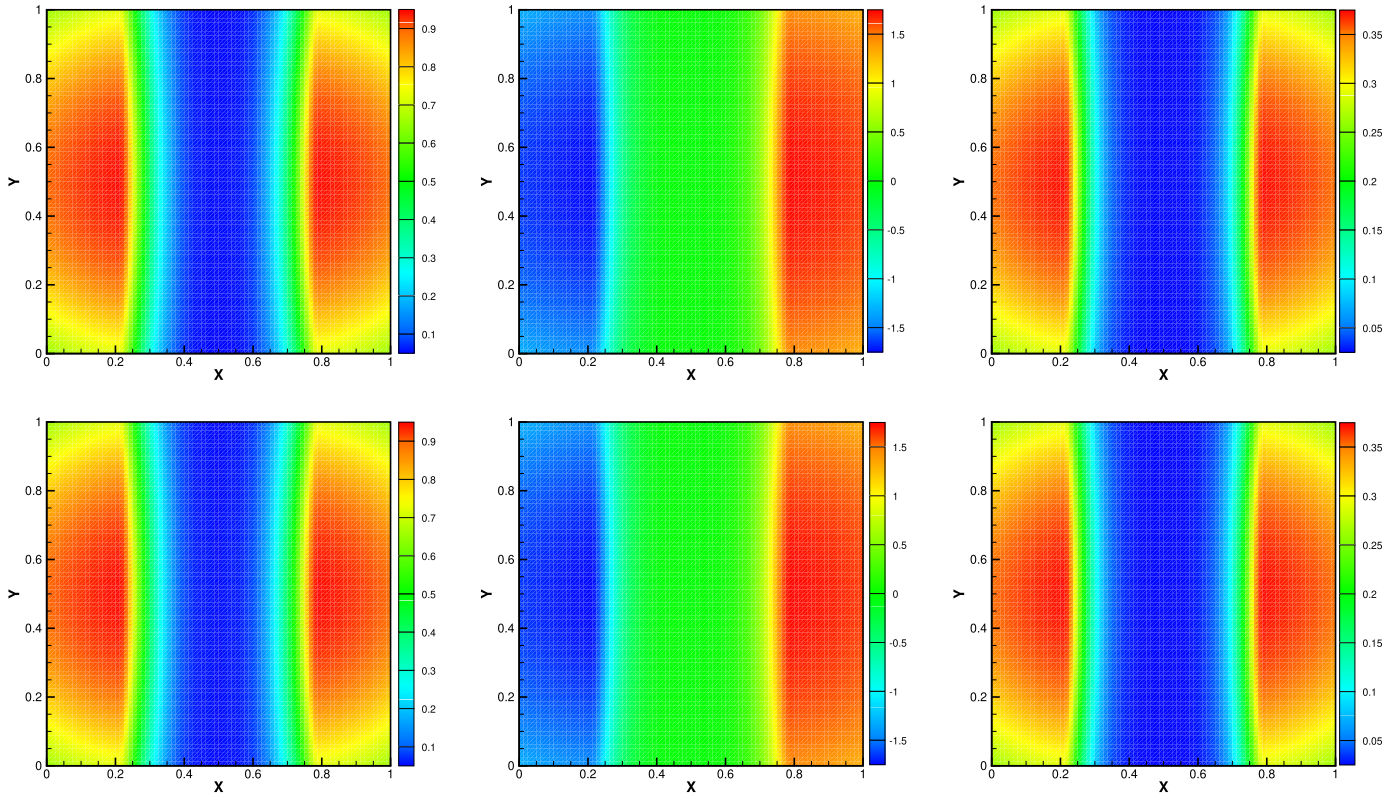

Fig. 5.9. Example 5.9, numerical solutions of density ρ (left), velocity u (mid) and pressure p (right) at $t = 0.1$ with 12800 triangles by using positivity-preserving well-balanced ALE-DG scheme. Top: the results of the scheme WB(H); Bottom: the results of the scheme WB(S).

Appendix A. Proof for Theorem 4.7

Since the TVD-RK methods are the convex combination of the Euler forward methods, we only need to show that this theorem holds for semi-discrete scheme (3.14) coupled with Euler forward time discretization, which takes the form

$$\frac{(1+\Delta t\nabla_{\boldsymbol{x}^n}\cdot\boldsymbol{\omega}^n)\Delta_{K^n}}{\Delta_{K^{n+1}}}\int_{K^{n+1}}\boldsymbol{U}_K^{n+1}\cdot\boldsymbol{\varphi}^{n+1}\mathrm{d}\boldsymbol{x}$$
$$=\int_{K^n}\boldsymbol{U}_K^n\cdot\boldsymbol{\varphi}^n\mathrm{d}\boldsymbol{x}+\Delta t\mathcal{L}_K^h(\boldsymbol{\omega}^n,\boldsymbol{U}^n,\boldsymbol{\varphi}^n,t^n). \tag{A.1}$$

By taking the test function to be 1, we can write the equation satisfied by $\bar{\boldsymbol{U}}_K^{n+1}$ according to (3.14) and decompose it into two parts

$$\begin{aligned}&(1+\Delta t\nabla_{\boldsymbol{x}^n}\cdot\boldsymbol{\omega}^n)\bar{\boldsymbol{U}}_K^{n+1}\\&=\bar{\boldsymbol{U}}_K^n+\lambda\Big(-\int_{\partial K^n}\hat{\boldsymbol{G}}\left(\boldsymbol{\omega},\boldsymbol{U}^{b,int_{K^n}},\boldsymbol{U}^{b,ext_{K^n}},\boldsymbol{n}\right)\mathrm{d}\boldsymbol{s}\\&\qquad+\int_{K^n}\boldsymbol{S}(\boldsymbol{U}^f,-\frac{\nabla p^{\tilde{e}}}{\rho^e})\mathrm{d}\boldsymbol{x}+\int_{\partial K^n}\boldsymbol{F}(\boldsymbol{U}^{\tilde{e},int_{K^n}})\cdot\boldsymbol{n}\mathrm{d}\boldsymbol{s}\Big)\\&=\boldsymbol{W}_1+\boldsymbol{W}_2,\end{aligned}$$

with

$$\boldsymbol{W}_1=\zeta\bar{\boldsymbol{U}}_K^n-\lambda\int_{\partial K^n}\hat{\boldsymbol{G}}\left(\boldsymbol{\omega},\boldsymbol{U}^{b,int_{K^n}},\boldsymbol{U}^{b,ext_{K^n}},\boldsymbol{n}\right)\mathrm{d}\boldsymbol{s}, \tag{A.2}$$

$$\boldsymbol{W}_2=\vartheta\bar{\boldsymbol{U}}_K^n+\lambda\left(\int_{K^n}\boldsymbol{S}(\boldsymbol{U}^f,-\frac{\nabla p^{\tilde{e}}}{\rho^e})\mathrm{d}\boldsymbol{x}+\int_{\partial K^n}\boldsymbol{F}(\boldsymbol{U}^{\tilde{e},int_{K^n}})\cdot\boldsymbol{n}\mathrm{d}\boldsymbol{s}\right), \tag{A.3}$$

where

$$\zeta=\frac{\hat{\alpha}_F}{\hat{\alpha}_0},\quad \vartheta=\frac{\hat{\alpha}_S}{\hat{\alpha}_0},\quad \text{satisfying } \zeta+\vartheta=1, \tag{A.4}$$

and $\lambda=\frac{\Delta t}{\Delta_{K^n}}$. Using Lemma 4.1, we only need to prove $\boldsymbol{W}_1,\ \boldsymbol{W}_2\in\mathcal{G}$. Since only the cell K^n is used in the following proof, we denote it by K for simplicity.

- **The proof of $\boldsymbol{W}_1\in\mathcal{G}$**

We use the quadrature rules introduced in Section 4.1 to rewrite the term $\boldsymbol{W}_1$:

$$\begin{aligned}\boldsymbol{W}_1=&\zeta\left(\sum_{\nu=1}^{d+1}\sum_{\mu=1}^{N}\tilde{\omega}_{F_K^\nu}^\mu\boldsymbol{U}^{n,int_K}\left(\tilde{\boldsymbol{x}}_{F_K^\nu}^\mu\right)+\sum_{\mu=1}^{\tilde{L}}\tilde{\omega}_K^\mu\boldsymbol{U}_K^n\left(\tilde{\boldsymbol{x}}_K^\mu\right)\right)\\&-\lambda\sum_{\nu=1}^{d+1}\sum_{\mu=1}^{N}\tilde{\varpi}_{F_K^\nu}^\mu\left|F_K^\nu\right|\hat{\boldsymbol{G}}\left(\boldsymbol{\omega},\boldsymbol{U}^{b,int_{K^n}},\boldsymbol{U}^{b,ext_{K^n}},\boldsymbol{n}\right)\\=&\zeta\sum_{\mu=1}^{\tilde{L}}\tilde{\omega}_K^\mu\boldsymbol{U}_K^n\left(\tilde{\boldsymbol{x}}_K^\mu\right)\\&+\sum_{\nu=1}^{d+1}\sum_{\mu=1}^{N}\zeta\tilde{\omega}_{F_K^\nu}^\mu\left(\boldsymbol{U}^{n,int_K}\left(\tilde{\boldsymbol{x}}_{F_K^\nu}^\mu\right)-\frac{1}{\hat{\alpha}_1}\boldsymbol{U}^{b,int_K}\left(\tilde{\boldsymbol{x}}_{F_K^\nu}^\mu\right)\right)\\&+\sum_{\nu=1}^{d+1}\sum_{\mu=1}^{N}\frac{\zeta\tilde{\omega}_{F_K^\nu}^\mu}{\hat{\alpha}_1}\Bigg(\boldsymbol{U}^{b,int_K}\left(\tilde{\boldsymbol{x}}_{F_K^\nu}^\mu\right)\\&\qquad-\frac{\hat{\alpha}_1\lambda\tilde{\varpi}_{F_K^\nu}^\mu\left|F_K^\nu\right|}{\zeta\tilde{\omega}_{F_K^\nu}^\mu}\hat{\boldsymbol{G}}\left(\boldsymbol{\omega},\boldsymbol{U}^{b,int_{K^n}},\boldsymbol{U}^{b,ext_{K^n}},\boldsymbol{n}\right)\Bigg),\end{aligned} \tag{A.5}$$

where $|F_K^\nu|$ denotes the area of edge F_K^ν. We have decomposed $\boldsymbol{W}_1$ into three parts. In order to show that $\boldsymbol{W}_1\in\mathcal{G}$, one can utilize the convexity of $\mathcal{G}$ and show that all three parts belong to the admissible set $\mathcal{G}$ via the following three claims.

1. $\boldsymbol{U}_K^n\left(\tilde{\boldsymbol{x}}_K^\mu\right)\in\mathcal{G}$.
   This is the assumption of the theorem.
2. $\boldsymbol{U}^{n,int_K}\left(\tilde{\boldsymbol{x}}_{F_K^\nu}^\mu\right)-\frac{1}{\hat{\alpha}_1}\boldsymbol{U}^{b,int_K}\left(\tilde{\boldsymbol{x}}_{F_K^\nu}^\mu\right)\in\mathcal{G}$.
   Since $1/\hat{\alpha}_1$ satisfies the constraint in Lemma 4.5, this claim follows from the conclusion of Lemma 4.5.
3. $\boldsymbol{U}^{b,int_K}\left(\tilde{\boldsymbol{x}}_{F_K^\nu}^\mu\right)-\frac{\hat{\alpha}_1\lambda\tilde{\varpi}_{F_K^\nu}^\mu\left|F_K^\nu\right|}{\zeta\tilde{\omega}_{F_K^\nu}^\mu}\hat{\boldsymbol{G}}\left(\boldsymbol{\omega},\boldsymbol{U}^{b,int_{K^n}},\boldsymbol{U}^{b,ext_{K^n}},\boldsymbol{n}\right)\in\mathcal{G}$.
   Using the definitions of $\hat{\alpha}_0$, $\hat{\alpha}_F$ and ζ, we first simplify the coefficient as

$$\frac{\hat{\alpha}_1\lambda\tilde{\varpi}_{F_K^\nu}^\mu\left|F_K^\nu\right|}{\zeta\tilde{\omega}_{F_K^\nu}^\mu}=\hat{\alpha}_1\frac{\Delta t}{\Delta_{K^n}}\frac{\hat{\alpha}_0}{\hat{\alpha}_F}\frac{\tilde{\varpi}_{F_K^\nu}^\mu\left|F_K^\nu\right|}{\tilde{\omega}_{F_K^\nu}^\mu}=\hat{\alpha}_0\Delta t\frac{\hat{\alpha}_1}{\hat{\alpha}_F}\frac{\tilde{\varpi}_{F_K^\nu}^\mu\left|F_K^\nu\right|}{\tilde{\omega}_{F_K^\nu}^\mu\Delta_{K^n}}\le\frac{1}{2\alpha},\tag{A.6}$$

   and then apply Lemma 4.4 to prove the above claim.

Now combining that the parameters ζ, λ and the quadrature weights $\tilde{\omega}_{F_K^\nu}^\mu$, $\tilde{\varpi}_{F_K^\nu}^\mu$, $\tilde{\omega}_K^\mu$ and the area of edge $|F_K^\nu|$ are all greater than 0, we can use Lemma 4.1 to prove that $\boldsymbol{W}_1\in\mathcal{G}$.

- **The proof of $\boldsymbol{W}_2\in\mathcal{G}$** (Same as the proof in [49, Proposition 4.5])

Notice that $\boldsymbol{m}^{\tilde{e},int_K}\equiv 0$ and

$$\boldsymbol{F}\left(\boldsymbol{U}^{\tilde{e},int_K}\right)=\begin{pmatrix}0\\(\gamma-1)E^{\tilde{e},int_K}I\\0\end{pmatrix},$$

which suggests that every component of $\boldsymbol{F}\left(\boldsymbol{U}^{\tilde{e},int_K}\right)$ is a polynomial in ∂K. Therefore it can be exactly integrated by the Gauss quadrature rule and one can use the integration by parts and the Gauss quadrature rule to rewrite $\boldsymbol{W}_2$ as

$$\begin{aligned}\boldsymbol{W}_2&=\vartheta\bar{\boldsymbol{U}}_K^n+\lambda\left(\int_K\boldsymbol{S}\left(\boldsymbol{U}^f,-\frac{\nabla p^{\tilde{e}}}{\rho^e}\right)\mathrm{d}\boldsymbol{x}+\int_K\nabla\cdot\boldsymbol{F}\left(\boldsymbol{U}^{\tilde{e}}\right)\mathrm{d}\boldsymbol{x}\right)\\&=\sum_{\mu=1}^L\hat{\omega}_K^\mu\Bigg(\vartheta\boldsymbol{U}_K^n\left(\hat{\boldsymbol{x}}_K^\mu\right)\\&\qquad+\Delta t\left(\nabla\cdot\boldsymbol{F}\left(\boldsymbol{U}_K^{\tilde{e}}\left(\hat{\boldsymbol{x}}_K^\mu\right)\right)+\boldsymbol{S}\left(\boldsymbol{U}_K^f\left(\hat{\boldsymbol{x}}_K^\mu\right),-\frac{\nabla p_K^{\tilde{e}}\left(\hat{\boldsymbol{x}}_K^\mu\right)}{\rho_K^e\left(\hat{\boldsymbol{x}}_K^\mu\right)}\right)\right)\Bigg).\end{aligned}$$

Since $\mathcal{G}$ is convex and all the quadrature weights are positive, it is sufficient to prove, for $\mu=1,\cdots,L$,

$$\begin{aligned}\boldsymbol{W}_2^\mu&=\vartheta\boldsymbol{U}_K^n\left(\hat{\boldsymbol{x}}_K^\mu\right)\\&\quad+\Delta t\left(\nabla\cdot\boldsymbol{F}\left(\boldsymbol{U}_K^{\tilde{e}}\left(\hat{\boldsymbol{x}}_K^\mu\right)\right)+\boldsymbol{S}\left(\boldsymbol{U}_K^f\left(\hat{\boldsymbol{x}}_K^\mu\right),-\frac{\nabla p_K^{\tilde{e}}\left(\hat{\boldsymbol{x}}_K^\mu\right)}{\rho_K^e\left(\hat{\boldsymbol{x}}_K^\mu\right)}\right)\right)\in\mathcal{G}.\end{aligned}$$

The first component of $\boldsymbol{W}_2^\mu$ reduces to $\vartheta\rho_K^n\left(\hat{\boldsymbol{x}}_K^\mu\right)$ which is automatically positive. In order to show that $\mathcal{E}\left(\boldsymbol{W}_2^\mu\right)>0$, we have

$$\begin{aligned}\mathcal{E}\left(\boldsymbol{W}_2^\mu\right)&=\vartheta E_K^n+\Delta t\boldsymbol{m}_K^f\cdot\frac{\nabla p_K^{\tilde{e}}}{\rho_K^e}-\left.\frac{\left\|\vartheta\boldsymbol{m}_K^n+\Delta t\left(\nabla p_K^{\tilde{e}}+\rho_K^f\frac{\nabla p_K^{\tilde{e}}}{\rho_j^e}\right)\right\|^2}{2\vartheta\rho_K^n}\right|_{\hat{\boldsymbol{x}}_K^\mu}\\&=\vartheta E_K^n+\Delta t\boldsymbol{m}_K^f\cdot\frac{\nabla p_K^{\tilde{e}}}{\rho_K^e}-\left.\frac{\left\|\vartheta\boldsymbol{m}_K^n+\Delta t\frac{\rho_K^n}{\rho_K^e}\nabla p_K^{\tilde{e}}\right\|^2}{2\vartheta\rho_K^n}\right|_{\hat{\boldsymbol{x}}_K^\mu}\\&=\vartheta(\rho e)_K^n+\Delta t\boldsymbol{m}_K^f\cdot\frac{\nabla p_K^{\tilde{e}}}{\rho_K^e}-\Delta t\frac{\boldsymbol{m}_K^n}{\rho_K^e}\cdot\nabla p_K^{\tilde{e}}-\left.\Delta t^2\frac{\left\|\frac{\rho_K^n}{\rho_K^e}\nabla p_K^{\tilde{e}}\right\|^2}{2\vartheta\rho_K^n}\right|_{\hat{\boldsymbol{x}}_K^\mu}\\&=\vartheta(\rho e)_K^n\left.\left(1-\Delta t^2\frac{\left\|\nabla p_K^{\tilde{e}}/\rho_K^e\right\|^2}{2\vartheta^2e_K^n}\right)\right|_{\hat{\boldsymbol{x}}_K^\mu},\end{aligned}$$

where $\rho^e+\rho^f=\rho^n$ is used in the second equality, and $\boldsymbol{m}^f=\boldsymbol{m}^n$ is used to derive the last equality. Following the definition of ϑ in (A.4) and $\hat{\alpha}_0$, $\hat{\alpha}_S$ in (4.22), we have

$$\Delta t^2\frac{\left\|\nabla p_K^{\tilde{e}}/\rho_K^e\right\|^2}{2\vartheta^2e_K^n}=(\hat{\alpha}_0\Delta t)^2\frac{\left\|\nabla p_K^{\tilde{e}}/\rho_K^e\right\|^2}{2\hat{\alpha}_S^2e_K^n}\le 1,$$

hence it follows that $\mathcal{E}\left(\boldsymbol{W}_2^\mu\right)\ge 0$, i.e., $\boldsymbol{W}_2\in\mathcal{G}$.

Appendix B. Proof for Theorem 4.8

Similar to the hydrostatic reconstruction case, we only need to prove this theorem for semi-discrete scheme (3.20) coupled with Euler forward time discretization taking the form of (A.1).

By taking the test function to be 1, we can write the equation satisfied by $\bar{\boldsymbol{U}}_K^{n+1}$ according to (3.20) and decompose it into two parts

$$\begin{aligned}&(1+\Delta t\nabla_{\boldsymbol{x}^n}\cdot\boldsymbol{\omega}^n)\bar{\boldsymbol{U}}_K^{n+1}\\&=\bar{\boldsymbol{U}}_K^n+\lambda\left(-\int_{\partial K^n}\hat{\boldsymbol{G}}\left(\boldsymbol{\omega},\boldsymbol{U}^{\tilde{b},int_{K^n}},\boldsymbol{U}^{\tilde{b},ext_{K^n}},\boldsymbol{n}\right)\mathrm{d}\boldsymbol{s}+\boldsymbol{S}_{K^n}^s\right)\\&=\boldsymbol{W}_1+\boldsymbol{W}_2,\end{aligned}$$

with

$$\boldsymbol{W}_1=\zeta\bar{\boldsymbol{U}}_K^n-\lambda\int_{\partial K^n}\hat{\boldsymbol{G}}\left(\boldsymbol{\omega},\boldsymbol{U}^{\tilde{b},int_{K^n}},\boldsymbol{U}^{\tilde{b},ext_{K^n}},\boldsymbol{n}\right)\mathrm{d}\boldsymbol{s},\tag{B.1}$$

$$\boldsymbol{W}_2=\vartheta\bar{\boldsymbol{U}}_K^n+\lambda S_{K^n}^*,\tag{B.2}$$

where $S_{K^n}^*$ denotes the source term approximation $\boldsymbol{S}_{K^n}^s$ in (3.19) with the test function $\boldsymbol{\varphi}=1$, and

$$\zeta=\frac{\tilde{\alpha}_F}{\tilde{\alpha}_0},\quad\vartheta=\frac{\tilde{\alpha}_S}{\tilde{\alpha}_0},\quad\text{satisfying }\zeta+\vartheta=1,\tag{B.3}$$

and $\lambda=\frac{\Delta t}{\Delta_{K^n}}$. Using Lemma 4.1, we only need to prove $\boldsymbol{W}_1$, $\boldsymbol{W}_2\in\mathcal{G}$. Since only the cell K^n is used in the following proof, we denote it by K for simplicity.

- **The proof of $\boldsymbol{W}_1\in\mathcal{G}$**
  The approach is similar to (A.5) and we write the specific form of $\boldsymbol{W}_1$ by using the quadrature rules:

$$\begin{aligned}\boldsymbol{W}_1=&\zeta\sum_{\mu=1}^{\bar{L}}\tilde{\omega}_K^\mu\boldsymbol{U}_K^n\left(\tilde{\boldsymbol{x}}_K^\mu\right)\\&+\sum_{\nu=1}^{d+1}\sum_{\mu=1}^N\zeta\tilde{\omega}_{F_K^\nu}^\mu\left(\boldsymbol{U}^{n,int_K}\left(\tilde{\boldsymbol{x}}_{F_K^\nu}^\mu\right)-\frac{1}{\tilde{\alpha}_1}\boldsymbol{U}^{\tilde{b},int_K}\left(\tilde{\boldsymbol{x}}_{F_K^\nu}^\mu\right)\right)\\&+\sum_{\nu=1}^{d+1}\sum_{\mu=1}^N\frac{\zeta\tilde{\omega}_{F_K^\nu}^\mu}{\tilde{\alpha}_1}\Bigg(\boldsymbol{U}^{\tilde{b},int_K}\left(\tilde{\boldsymbol{x}}_{F_K^\nu}^\mu\right)\\&\qquad-\frac{\tilde{\alpha}_1\lambda\tilde{\varpi}_{F_K^\nu}^\mu\left|F_K^\nu\right|}{\zeta\tilde{\omega}_{F_K^\nu}^\mu}\hat{\boldsymbol{G}}\left(\boldsymbol{\omega},\boldsymbol{U}^{\tilde{b},int_{K^n}},\boldsymbol{U}^{\tilde{b},ext_{K^n}},\boldsymbol{n}\right)\Bigg).\end{aligned}$$

  We have decomposed $\boldsymbol{W}_1$ into three parts. In order to show that $\boldsymbol{W}_1\in\mathcal{G}$, one can utilize the convexity of $\mathcal{G}$ and show that all three parts belong to the admissible set $\mathcal{G}$ via the following three claims.

1. $\boldsymbol{U}_K^n\left(\tilde{\boldsymbol{x}}_K^\mu\right) \in \mathcal{G}$.
   This is the assumption of the theorem.
2. $\boldsymbol{U}^{n,int_K}\left(\tilde{\boldsymbol{x}}_{F_K^\nu}^\mu\right) - \frac{1}{\tilde{\alpha}_1}\boldsymbol{U}^{\tilde{b},int_K}\left(\tilde{\boldsymbol{x}}_{F_K^\nu}^\mu\right) \in \mathcal{G}$.
   Since

$$\boldsymbol{U}^{\tilde{b},int_K} = \frac{p^c}{p^{\tilde{b},int_K}}\boldsymbol{U}^{n,int_K}, \text{ and } \tilde{\alpha}_1 \geq \frac{p^c}{p^{\tilde{b},int_K}} \text{ for } \boldsymbol{x} \in \mathbb{Q}_K, \tag{B.4}$$

   we have $1 - \frac{1}{\tilde{\alpha}_1}\frac{p^c}{p^{\tilde{b},int_K}} \geq 0$, which proves the claim.
3. $\boldsymbol{U}^{\tilde{b},int_K}\left(\tilde{\boldsymbol{x}}_{F_K^\nu}^\mu\right) - \frac{\tilde{\alpha}_1\lambda\tilde{\varpi}_{F_K^\nu}^\mu\left|F_K^\nu\right|}{\zeta\tilde{\omega}_{F_K^\nu}^\mu}\hat{\boldsymbol{G}}\left(\boldsymbol{\omega}, \boldsymbol{U}^{\tilde{b},int_{K^n}}, \boldsymbol{U}^{\tilde{b},ext_{K^n}}, \boldsymbol{n}\right) \in \mathcal{G}$.
   Similar simplification in (A.6) can be carried out by using the definitions of $\tilde{\alpha}_0$, $\tilde{\alpha}_F$ and ζ:

$$\frac{\tilde{\alpha}_1\lambda\tilde{\varpi}_{F_K^\nu}^\mu\left|F_K^\nu\right|}{\zeta\tilde{\omega}_{F_K^\nu}^\mu} = \tilde{\alpha}_1\frac{\Delta t}{\Delta_{K^n}}\frac{\tilde{\alpha}_0}{\tilde{\alpha}_F}\frac{\tilde{\varpi}_{F_K^\nu}^\mu\left|F_K^\nu\right|}{\tilde{\omega}_{F_K^\nu}^\mu} = \tilde{\alpha}_0\Delta t\frac{\tilde{\alpha}_1}{\tilde{\alpha}_F}\frac{\tilde{\varpi}_{F_K^\nu}^\mu\left|F_K^\nu\right|}{\tilde{\omega}_{F_K^\nu}^\mu\mu\Delta_{K^n}} \leq \frac{1}{2\alpha}. \tag{B.5}$$

   Therefore, we use Lemma 4.4 to prove the above claim.

Now combining that the parameters ζ, λ and the quadrature weights $\tilde{\omega}_{F_K^\nu}^\mu$, $\tilde{\varpi}_{F_K^\nu}^\mu$, $\tilde{\omega}_K^\mu$ and the area of edge $|F_K^\nu|$ are all greater than 0, we can use Lemma 4.1 to prove that $\boldsymbol{W}_1 \in \mathcal{G}$.

- **The proof of $\boldsymbol{W}_2 \in \mathcal{G}$** (Similar to the proof in [38, Theorems 3.3 and 4.3])

We apply integration by parts in (3.19) to simplify the integration:

$$S_K^* = \begin{pmatrix} 0 \\ \int_K -\rho\frac{\nabla p^e}{\rho^e}\mathrm{d}\boldsymbol{x} \\ \int_K -\boldsymbol{m}\cdot\frac{\nabla p^e}{\rho^e}\mathrm{d}\boldsymbol{x} \end{pmatrix} + \begin{pmatrix} 0 \\ \frac{\bar{\rho}}{\bar{\rho}^e}\int_{\partial K}[p]^{e,K}\boldsymbol{n}\mathrm{d}\boldsymbol{s} \\ \frac{\bar{\boldsymbol{m}}}{\bar{\rho}^e}\cdot\int_{\partial K}[p]^{e,K}\boldsymbol{n}\mathrm{d}\boldsymbol{s} \end{pmatrix} = \boldsymbol{W}_2^1 + \boldsymbol{W}_2^2.$$

With these notations, $\boldsymbol{W}_2$ can be rewritten as follows

$$\begin{aligned}\boldsymbol{W}_2 &= \vartheta_1\bar{\boldsymbol{U}} + \lambda\boldsymbol{W}_2^1 + \vartheta_2\bar{\boldsymbol{U}} + \lambda\boldsymbol{W}_2^2 \\ &= \sum_{\mu=1}^{L}\hat{\omega}_\mu\left(\vartheta_1\boldsymbol{U}_K^n(\hat{\boldsymbol{x}}_K^\mu) + \Delta t\boldsymbol{S}\left(\boldsymbol{U}_K^n(\hat{\boldsymbol{x}}_K^\mu), -\frac{\nabla p_K^e(\hat{\boldsymbol{x}}_K^\mu)}{\rho_K^e(\hat{\boldsymbol{x}}_K^\mu)}\right)\right) \\ &\quad + \vartheta_2\bar{\boldsymbol{U}}_K^n + \frac{\lambda}{\bar{\rho}^e}\begin{pmatrix} 0 \\ \bar{\rho}\int_{\partial K}[p]^{e,K}\boldsymbol{n}\mathrm{d}\boldsymbol{s} \\ \bar{\boldsymbol{m}}\cdot\int_{\partial K}[p]^{e,K}\boldsymbol{n}\mathrm{d}\boldsymbol{s}\end{pmatrix}\end{aligned}$$

where $\vartheta_1 = \frac{\tilde{\alpha}_S^1}{\tilde{\alpha}_0}$, $\vartheta_2 = \frac{\tilde{\alpha}_S^2}{\tilde{\alpha}_0}$, and $\vartheta = \vartheta_1 + \vartheta_2$. We first claim that

$$\vartheta_1\boldsymbol{U}_K^n(\hat{\boldsymbol{x}}_K^\mu) + \Delta t\boldsymbol{S}\left(\boldsymbol{U}_K^n(\hat{\boldsymbol{x}}_K^\mu), -\frac{\nabla p_K^e(\hat{\boldsymbol{x}}_K^\mu)}{\rho_K^e(\hat{\boldsymbol{x}}_K^\mu)}\right) \in \mathcal{G}, \tag{B.6}$$

which follows from Lemma 4.6 and the fact that the coefficient ϑ_1 satisfies

$$\vartheta_1 = \frac{\tilde{\alpha}_S^1}{\tilde{\alpha}_0} \geq \Delta t\frac{||\nabla p_K^e(\hat{\boldsymbol{x}}_K^\mu)/\rho_K^e(\hat{\boldsymbol{x}}_K^\mu)||}{\sqrt{2e_K^n(\hat{\boldsymbol{x}}_K^\mu)}}.$$

Similarly, we conclude that

$$\vartheta_2\bar{\boldsymbol{U}}_K^n + \frac{\lambda}{\bar{\rho}^e}\begin{pmatrix} 0 \\ \bar{\rho}\int_{\partial K}[p]^{e,K}\boldsymbol{n}\mathrm{d}\boldsymbol{s} \\ \bar{\boldsymbol{m}}\cdot\int_{\partial K}[p]^{e,K}\boldsymbol{n}\mathrm{d}\boldsymbol{s}\end{pmatrix} \in \mathcal{G}, \tag{B.7}$$

which again follows from Lemma 4.6 and the fact that the coefficient ϑ_2 satisfies

$$\vartheta_2 = \frac{\tilde{\alpha}_S^2}{\tilde{\alpha}_0} \geq \frac{\lambda||\int_{\partial K}[p]^{e,K}\boldsymbol{n}\mathrm{d}\boldsymbol{s}||}{\bar{\rho}^e\sqrt{2\bar{e}_K^n}}.$$

Therefore, we can apply Lemma 4.1 to conclude that $\boldsymbol{W}_2 \in \mathcal{G}$.

References

[1] E. Audusse, F. Bouchut, M.-O. Bristeau, R. Klein, B.t. Perthame, A fast and stable well-balanced scheme with hydrostatic reconstruction for shallow water flows, SIAM J. Sci. Comput. 25 (6) (2004) 2050–2065.
[2] J. Badwaik, P. Chandrashekar, C. Klingenberg, Single-step arbitrary Lagrangian–Eulerian discontinuous Galerkin method for 1-D Euler equations, Commun. Appl. Math. Comput. 2 (2020) 541–579.
[3] D.S. Bale, R.J. Leveque, S. Mitran, J.A. Rossmanith, A wave propagation method for conservation laws and balance laws with spatially varying flux functions, SIAM J. Sci. Comput. 24 (3) (2003) 955–978.
[4] P. Batten, N. Clarke, C. Lambert, D.M. Causon, On the choice of wavespeeds for the HLLC Riemann solver, SIAM J. Sci. Comput. 18 (6) (1997) 1553–1570.
[5] A. Bermudez, M.E. Vazquez, Upwind methods for hyperbolic conservation laws with source terms, Comput. Fluids 23 (8) (1994) 1049–1071.
[6] S. Brenner, R. Scott, The Mathematical Theory of Finite Element Methods, vol. 15, Springer Science & Business Media, 2007.
[7] M.J. Castro, C. Parés, Well-balanced high-order finite volume methods for systems of balance laws, J. Sci. Comput. 82 (2) (2020) 1–48.
[8] P. Chandrashekar, C. Klingenberg, A second order well-balanced finite volume scheme for Euler equations with gravity, SIAM J. Sci. Comput. 37 (3) (2015) B382–B402.
[9] P. Chandrashekar, M. Zenk, Well-balanced nodal discontinuous Galerkin method for Euler equations with gravity, J. Sci. Comput. 71 (3) (2017) 1062–1093.
[10] J. Cheng, C.-W. Shu, Positivity-preserving Lagrangian scheme for multi-material compressible flow, J. Comput. Phys. 257 (2014) 143–168.
[11] J. Donea, S. Giuliani, J.-P. Halleux, An arbitrary Lagrangian-Eulerian finite element method for transient dynamic fluid-structure interactions, Comput. Methods Appl. Mech. Eng. 33 (1–3) (1982) 689–723.
[12] J. Donea, A. Huerta, J.-P. Ponthot, A. Rodríguez-Ferran, Arbitrary Lagrangian–Eulerian methods, in: Encyclopedia of Computational Mechanics, second edition, 2017, pp. 1–23.
[13] B. Einfeldt, C.-D. Munz, P.L. Roe, B. Sjögreen, On Godunov-type methods near low densities, J. Comput. Phys. 92 (2) (1991) 273–295.
[14] P. Fu, G. Schnücke, Y. Xia, Arbitrary Lagrangian-Eulerian discontinuous Galerkin method for conservation laws on moving simplex meshes, Math. Comput. 88 (319) (2019) 2221–2255.
[15] E. Gaburro, M.J. Castro, M. Dumbser, Well-balanced arbitrary-Lagrangian-Eulerian finite volume schemes on moving nonconforming meshes for the Euler equations of gas dynamics with gravity, Mon. Not. R. Astron. Soc. 477 (2) (2018) 2251–2275.
[16] J.M. Gallardo, C. Parés, M. Castro, On a well-balanced high-order finite volume scheme for shallow water equations with topography and dry areas, J. Comput. Phys. 227 (1) (2007) 574–601.
[17] S. Gottlieb, C.-W. Shu, E. Tadmor, Strong stability-preserving high-order time discretization methods, SIAM Rev. 43 (1) (2001) 89–112.
[18] J.-L. Guermond, M. Nazarov, B. Popov, I. Tomas, Second-order invariant domain preserving approximation of the Euler equations using convex limiting, SIAM J. Sci. Comput. 40 (5) (2018) A3211–A3239.
[19] W. Huang, R.D. Russell, Adaptive Moving Mesh Methods, vol. 174, Springer Science & Business Media, 2010.
[20] T.J. Hughes, W.K. Liu, T.K. Zimmermann, Lagrangian-Eulerian finite element formulation for incompressible viscous flows, Comput. Methods Appl. Mech. Eng. 29 (3) (1981) 329–349.
[21] R. Käppeli, S. Mishra, Well-balanced schemes for the Euler equations with gravitation, J. Comput. Phys. 259 (2014) 199–219.
[22] R. Käppeli, S. Mishra, A well-balanced finite volume scheme for the Euler equations with gravitation-the exact preservation of hydrostatic equilibrium with arbitrary entropy stratification, Astron. Astrophys. 587 (2016) A94.
[23] C. Klingenberg, G. Puppo, M. Semplice, Arbitrary order finite volume well-balanced schemes for the Euler equations with gravity, SIAM J. Sci. Comput. 41 (2) (2019) A695–A721.
[24] C. Klingenberg, G. Schnücke, Y. Xia, Arbitrary Lagrangian-Eulerian discontinuous Galerkin method for conservation laws: analysis and application in one dimension, Math. Comput. 86 (305) (2017) 1203–1232.
[25] A. Kurganov, Finite-volume schemes for shallow-water equations, Acta Numer. 27 (2018) 289–351.
[26] R.J. LeVeque, Balancing source terms and flux gradients in high-resolution Godunov methods: the quasi-steady wave-propagation algorithm, J. Comput. Phys. 146 (1) (1998) 346–365.
[27] R.J. LeVeque, D.S. Bale, Wave propagation methods for conservation laws with source terms, in: Hyperbolic Problems: Theory, Numerics, Applications, Springer, 1999, pp. 609–618.
[28] G. Li, Y. Xing, High order finite volume WENO schemes for the Euler equations under gravitational fields, J. Comput. Phys. 316 (2016) 145–163.
[29] G. Li, Y. Xing, Well-balanced discontinuous Galerkin methods with hydrostatic reconstruction for the Euler equations with gravitation, J. Comput. Phys. 352 (2018) 445–462.
[30] I. Lomtev, R. Kirby, G. Karniadakis, A discontinuous Galerkin ALE method for compressible viscous flows in moving domains, J. Comput. Phys. 155 (1) (1999) 128–159.

[31] H. Luo, J.D. Baum, R. Löhner, On the computation of multi-material flows using ALE formulation, J. Comput. Phys. 194 (1) (2004) 304–328.
[32] V.-T. Nguyen, An arbitrary Lagrangian–Eulerian discontinuous Galerkin method for simulations of flows over variable geometries, J. Fluids Struct. 26 (2) (2010) 312–329.
[33] C. Parés, C. Parés-Pulido, Well-balanced high-order finite difference methods for systems of balance laws, J. Comput. Phys. 425 (2021) 109880.
[34] P.-O. Persson, J. Bonet, J. Peraire, Discontinuous Galerkin solution of the Navier–Stokes equations on deformable domains, Comput. Methods Appl. Mech. Eng. 198 (17–20) (2009) 1585–1595.
[35] B. Perthame, C.-W. Shu, On positivity preserving finite volume schemes for Euler equations, Numer. Math. 73 (1) (1996) 119–130.
[36] A. Thomann, M. Zenk, C. Klingenberg, A second-order positivity-preserving well-balanced finite volume scheme for Euler equations with gravity for arbitrary hydrostatic equilibria, Int. J. Numer. Methods Fluids 89 (11) (2019) 465–482.
[37] D. Varma, P. Chandrashekar, A second-order, discretely well-balanced finite volume scheme for Euler equations with gravity, Comput. Fluids 181 (2019) 292–313.
[38] K. Wu, Y. Xing, Uniformly high-Order structure-preserving discontinuous Galerkin methods for Euler equations with gravitation: positivity and well-balancedness, SIAM J. Sci. Comput. 43 (1) (2021) A472–A510.
[39] Y. Xing, Exactly well-balanced discontinuous Galerkin methods for the shallow water equations with moving water equilibrium, J. Comput. Phys. 257 (2014) 536–553.
[40] Y. Xing, C.-W. Shu, A new approach of high order well-balanced finite volume WENO schemes and discontinuous Galerkin methods for a class of hyperbolic systems with source terms, Commun. Comput. Phys. 1 (1) (2006) 100–134.
[41] Y. Xing, C.-W. Shu, High order well-balanced finite volume WENO schemes and discontinuous Galerkin methods for a class of hyperbolic systems with source terms, J. Comput. Phys. 214 (2) (2006) 567–598.
[42] Y. Xing, C.-W. Shu, High order well-balanced WENO scheme for the gas dynamics equations under gravitational fields, J. Sci. Comput. 54 (2) (2013) 645–662.
[43] Y. Xing, C.-W. Shu, A survey of high order schemes for the shallow water equations, J. Math. Study 47 (3) (2014) 221–249.
[44] Y. Xing, X. Zhang, C.-W. Shu, Positivity-preserving high order well-balanced discontinuous Galerkin methods for the shallow water equations, Adv. Water Resour. 33 (12) (2010) 1476–1493.
[45] T. Xiong, J.-M. Qiu, Z. Xu, Parametrized positivity preserving flux limiters for the high order finite difference WENO scheme solving compressible Euler equations, J. Sci. Comput. 67 (3) (2016) 1066–1088.
[46] Z. Xu, Parametrized maximum principle preserving flux limiters for high order schemes solving hyperbolic conservation laws: one-dimensional scalar problem, Math. Comput. 83 (289) (2014) 2213–2238.
[47] Z. Xu, X. Zhang, Bound-preserving high-order schemes, in: Handbook of Numerical Analysis, vol. 18, Elsevier, 2017, pp. 81–102.
[48] W. Zhang, Y. Xia, Y. Xu, Positivity-preserving well-balanced arbitrary Lagrangian–Eulerian discontinuous Galerkin methods for the shallow water equations, J. Sci. Comput. 88 (3) (2021) 1–43.
[49] W. Zhang, Y. Xing, Y. Xia, Y. Xu, High-order positivity-preserving well-balanced discontinuous Galerkin methods for Euler equations with gravitation on unstructured meshes, Commun. Comput. Phys. 31 (2022) 771–815.
[50] X. Zhang, C.-W. Shu, On positivity-preserving high order discontinuous Galerkin schemes for compressible Euler equations on rectangular meshes, J. Comput. Phys. 229 (23) (2010) 8918–8934.
[51] X. Zhang, C.-W. Shu, Positivity-preserving high order discontinuous Galerkin schemes for compressible Euler equations with source terms, J. Comput. Phys. 230 (4) (2011) 1238–1248.
[52] X. Zhang, Y. Xia, C.-W. Shu, Maximum-principle-satisfying and positivity-preserving high order discontinuous Galerkin schemes for conservation laws on triangular meshes, J. Sci. Comput. 50 (1) (2012) 29–62.